---

**Article:**

Mahato, S. orcid.org/0000-0002-1204-3185, Martínez de Irujo Labalde, X., Grievson, H. et al. (6 more authors) (2025) The role of Fe(IV)-O anion redox centers in the electrochemical behavior of Al- and Ga-doped T-LiFeO2. Chemistry of Materials, 37 (9). pp. 3171-3184. ISSN 0897-4756

https://doi.org/10.1021/acs.chemmater.4c03322

---

CHEMISTRY OF MATERIALS



pubs.acs.org/cm
Article

# The Role of Fe(IV)-O Anion Redox Centers in the Electrochemical Behavior of Al- and Ga-Doped T-$LiFeO_2$

Suraj Mahato, Xabier Martínez de Irujo Labalde, Heather Grievson, Josie-May Mortimer, Samuel G. Booth, Ashok Menon, Louis F. Piper, Serena Cussen, and Michael A. Hayward*

Cite This: *Chem. Mater.* 2025, 37, 3171−3184
Read Online



**ABSTRACT:** The high natural abundance and low toxicity of iron oxides provide a strong motivation to develop iron-based lithium-ion battery cathode materials. T-$LiFeO_2$ adopts a cation-ordered wurtzite structure consisting of apex-linked $LiO_4$ and $FeO_4$ tetrahedra. Chemical or electrochemical lithium extraction rapidly converts T-$LiFeO_2$ to the spinel $LiFe_5O_8$ and leads to poor energy storage performance. We have investigated the role of Al and Ga substitution on the stability of T-$LiFeO_2$. Partial substitution of Fe by Al leads to the formation of cation-disordered solid solutions. In contrast, neutron diffraction data reveal that the Ga-substituted phase $LiFe_{0.5}Ga_{0.5}O_2$ adopts an Fe/Ga cation-ordered structure. Chemical delithiation of $LiFe_{1-x}M_xO_2$ phases reveals that 25% Al or 50% Ga substitution stabilizes the T-$LiFe_{1-x}M_xO_2$ phases with respect to spinel conversion. The delithiated phases show no evidence of cation migration or oxygen loss. However, Fe-XANES, O-XAS, and O-RIXS data indicate that lithium extraction does not proceed via simple oxidation of $Fe^{3+}$ to $Fe^{4+}$ but rather via an anion redox process involving the formation of localized "$Fe^{IV}$−O" centers. Electrochemical data indicate that the formation of $Fe^{IV}$−O centers is irreversible, and so these oxidized species accumulate with continued electrochemical cycling, leading to a rapid decline in energy storage capacity. The electrochemical behavior of $LiFe_{0.5}Al_{0.5}O_2$ and $LiFe_{0.5}Ga_{0.5}O_2$ is discussed in terms of their crystal chemistry to account for the differing electrochemical performance of the Al- and Ga-substituted materials.

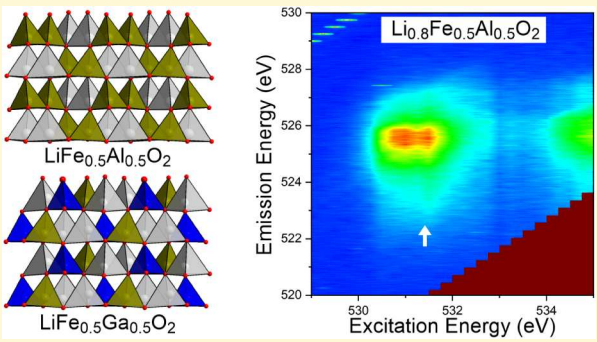




## ■ INTRODUCTION

Lithium-ion batteries provide high-energy density power sources for a wide range of technologies.[1−3] However, the majority of the currently commercialized lithium-ion battery systems contain large amounts of cobalt and nickel − two rare, expensive and toxic elements. If lithium-ion battery systems are to be widely utilized in applications such as grid-scale energy storage of renewable power generation or in electric vehicles, the use of these elements will need to be minimized and more abundant, more sustainable alternatives developed.[4,5]

The high abundance, low toxicity and low cost of iron oxides provide a strong motivation to develop iron-based lithium-ion cathode systems. However, there are a number of aspects of the chemistry of complex iron oxides which make this challenging. For example, it would be desirable to utilize the high potential of the $Fe^{III}/Fe^{IV}$ redox couple in Fe-based cathodes to maximize their energy storage density. However, while it is possible to prepare a variety of $Fe^{4+}$ containing oxide phases,[6,7] oxidative delithiation of $Fe^{III}$ oxides is observed to lead to a variety of "anion redox" processes in which the oxide ions in the material become partially oxidized in addition to, or instead of, simple oxidation of $Fe^{3+}$ to $Fe^{4+}$.[8−11] This involvement of the oxide ions in the electrochemical charging of Fe-based cathodes appears to be undesirable as it often leads to irreversible cathode oxidation and/or release of oxygen gas.

A further undesirable feature of Fe-cathode materials is their tendency to undergo large-scale cation migration during charge and discharge cycles. This deleterious behavior can be attributed to the high-spin S = $^5/_2$ electronic configuration of $Fe^{3+}$ which has no strong ligand-field-driven preference for any particular coordination geometry, in contrast to S = 2 $Fe^{4+}$ or S = 2 $Fe^{2+}$ centers. This, combined with the large change in ionic radius of $Fe^{3+}$ on oxidation or reduction ($Fe^{2+}$: 0.78 Å, $Fe^{3+}$: 0.645 Å, $Fe^{4+}$: 0.585Å)[12] provides a strong driving force for the structural reorganization of Fe-based cathodes during electrochemical cycling.

$LiFeO_2$ can be prepared with a number of different crystal structures.[13,14] For example, the most stable form at high temperature, $\alpha$-$LiFeO_2$, can be prepared directly from $Li_2CO_3$

Received: December 5, 2024
Revised: April 17, 2025
Accepted: April 17, 2025
Published: April 24, 2025





https://doi.org/10.1021/acs.chemmater.4c03322
*Chem. Mater.* 2025, 37, 3171−3184

and $Fe_2O_3$ at 700 °C and adopts a disordered rock salt structure,[15,16] which can be converted to the cation-ordered polymorph, $\gamma$-$LiFeO_2$, by annealing at 600 °C.[17,18] However, both these phases exhibit slow lithium insertion/extraction kinetics unless they are prepared in nanoparticulate form.[19,20] Additional metastable polymorphs can be prepared by utilizing low-temperature synthesis methods. For example, by reacting $\gamma$-FeOOH and LiOH the "corrugated layer" phase can be prepared,[14,21] or the 'O3′-$LiFeO_2$ or T-$LiFeO_2$ polymorphs prepared via Li-for-Na cation exchange from $\alpha$-$NaFeO_2$ and $\beta$-$NaFeO_2$ respectively.[22,23] However, while these metastable forms of $LiFeO_2$ can show significant electrochemical activity, detailed analysis reveals that during the first lithium deintercalation cycle these materials (along with $\alpha$-$LiFeO_2$ and $\gamma$-$LiFeO_2$) are converted to the spinel $LiFe_5O_8$,[16,23−26] by a combination of cation migration and oxygen loss, as described above. Subsequent electrochemical activity of these materials then most likely occurs via cycling between $LiFe_5O_8$ and $Li_3Fe_5O_8$.[27]

Recently we have been studying a series of Li−Fe-M-O ($M$ = In, Sb, Te) phases which adopt $LiSbO_3$-related crystal structures based on hexagonal close packed arrays of oxide ions. We observed that partial substitution of indium for iron in the lithium insertion cathode materials $LiFe_2SbO_6$ and $Li_3Fe_3Te_2O_{12}$ can suppress cation migration during charge−discharge cycles and enhance the long-term cyclability of the $Fe^{II/III}$ redox couple in these phases.[28,29]

Building on this work we now report a study on the effect of aluminum and gallium substitution on the structural and electrochemical behavior of T-$LiFeO_2$.[23] This metastable phase, first reported by Armstrong et al., is prepared via Li-for-Na cation exchange from $\beta$-$NaFeO_2$ and adopts a cation-ordered wurtzite structure consisting of apex linked $FeO_4$ and $NaO_4$ tetrahedra, as shown in Figure 1, again based on a hexagonally close packed oxygen framework. Previous studies show that T-$LiFeO_2$, like other $LiFeO_2$ polymorphs, rapidly converts to $LiFe_5O_8$ on electrochemical cycling. Here we show that, at sufficient levels of substitution, T-$LiFe_{1-x}M_xO_2$ ($M$ = Al, Ga) phases are stable with respect to spinel conversion, allowing their electrochemical behavior to be studied in detail.

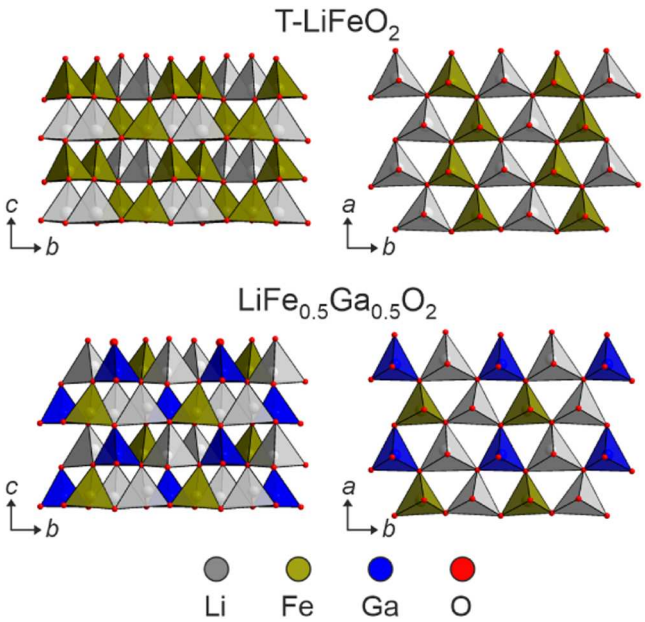


**Figure 1.** Crystal structures of T-$LiFeO_2$ and $LiFe_{0.5}Ga_{0.5}O_2$.

## ■ EXPERIMENTAL SECTION

**Synthesis of $NaFe_{1-x}M_xO_2$ ($M$ = Al, Ga).** Samples of $NaFe_{1-x}M_xO_2$ ($M$ = Al, Ga) were prepared by grinding together suitable quantities of $Fe_2O_3$ (99.995%), $Al_2O_3$ (99.995%) and $Ga_2O_3$ (99.999%) with a 10% excess of $Na_2CO_3$ (99.997%). $NaFe_{1-x}Al_xO_2$ samples were heated at 750 °C for 12 h before being reground, pressed into pellets and heated for multiple 12 h periods at 1100 °C until they were observed to form a single phase by powder X-ray diffraction (PXRD). $NaFe_{1-x}Ga_xO_2$ samples were heated at 750 °C for 12 h before being reground, pressed into pellets and heated for multiple 12 h periods at 900 °C until they were observed to form a single phase by PXRD.

**Synthesis of $LiFe_{1-x}M_xO_2$ ($M$ = Al, Ga).** $LiFe_{1-x}M_xO_2$ ($M$ = Al, Ga) phases were prepared by Li-for-Na cation exchange from the corresponding $NaFe_{1-x}M_xO_2$ phases using a method adapted from Armstrong et al.[23] Specifically, samples of $NaFe_{1-x}M_xO_2$ and 10 mol-equivalents of LiBr were added to a round bottomed flask fitted with a condenser, containing $n$-hexanol. The suspension was then heated at 165 °C for 12 h with constant stirring, before the solid was filtered from the suspension and washed with methanol. PXRD data collected from material at this point exhibited broad diffraction reflections indicative of partial cation exchange. To complete the cation exchange reaction, the dry products of the LiBr/$n$-hexanol process were ground with 10 mol-equivalents of LiBr and then heated in air at 200 °C for 48 h. The resulting material was then washed in methanol to remove the excess LiBr and filtered to dryness.

**Chemical Lithiation of $LiFe_{1-x}M_xO_2$ ($M$ = Al, Ga).** Small samples (∼200 mg) of $LiFe_{1-x}M_xO_2$ ($M$ = Al, Ga) phases were placed in Schlenk tubes, under a nitrogen atmosphere and ∼ 6 mL of a 1.6 M solution of $n$-BuLi in hexanes was added via a canula to achieve an approximate 1:5 molar ratio of $LiFe_{1-x}M_xO_2$:$n$-BuLi. The Schlenk tubes were then sealed under nitrogen, and the suspensions stirred for 48 h at room temperature, before being filtered and the solid materials washed with toluene, before being filtered to dryness. Lithiated samples were subsequently stored and measured under inert conditions. A sample for analysis by neutron diffraction was prepared by performing the same procedure on ∼ 2 g of $LiFe_{0.5}Ga_{0.5}O_2$ using 2 portions of 15 mL of a 1.6 M solution of $n$-BuLi in hexanes.

To assess the reversibility of lithium insertion, carefully weighed samples of $Li_{1+\delta}Fe_{1-x}M_xO_2$ were added to Schlenk tubes containing known quantities of $I_2$ dissolved in acetonitrile, and stirred at room temperature under nitrogen for 1 d. After this time the solid samples were recovered by filtration and the quantity of iodine remaining was determined by titration with thiosulfate.

**Chemical Delithiation of $LiFe_{1-x}M_xO_2$ ($M$ = Al, Ga).** Small samples (∼200 mg) of $LiFe_{1-x}M_xO_2$ ($M$ = Al, Ga) were added to small Schlenk tubes containing ∼ 500 mg of $NO_2BF_4$ (95%) in 10 mL of acetonitrile under a nitrogen atmosphere, to achieve an approximate 1:5 molar ratio of $LiFe_{1-x}M_xO_2$:$NO_2BF_4$. The Schlenk tubes were then sealed and the suspensions stirred and heated at 50 °C for 7 d. The reaction mixtures were then filtered and washed with clean acetonitrile under nitrogen, before being dried under vacuum. Delithiated samples were subsequently stored and measured


https://doi.org/10.1021/acs.chemmater.4c03322
Chem. Mater. 2025, 37, 3171−3184

under inert conditions. Samples for analysis by neutron diffraction were prepared by performing the same procedure on ∼ 2 g of $LiFe_{0.5}Al_{0.5}O_2$ and $LiFe_{0.5}Ga_{0.5}O_2$ using 2 portions of 2 g $NO_2BF_4$ in 20 mL of acetonitrile.

To assess the reversibility of the lithium extraction from $LiFe_{1-x}M_xO_2$ phases, deintercalated samples were treated with LiI, by adding carefully weighed samples of ∼ 50 mg of $Li_{1-\delta}Fe_{1-x}M_xO_2$ to Schlenk tubes containing 300 mg of LiI dissolved in 10 mL of acetonitrile, under nitrogen. The Schlenk tubes were then sealed and the contents stirred and heated to 50 °C for 3 d. After this time the solid sample was recovered by filtration and the quantity of iodine released into the liquid was determined by titration with thiosulfate.

**Characterization.** Reaction progress monitoring and initial structural characterization was performed using laboratory powder X-ray diffraction (PXRD) data collected using a PANalytical X'pert diffractometer incorporating an X'celerator position-sensitive detector (monochromatic Cu K$\alpha$1 radiation). High-resolution synchrotron X-ray powder diffraction (SXRD) data were collected using the I11 instrument at the Diamond Light Source Ltd. Diffraction patterns were collected using Si-calibrated X-rays with an approximate wavelength of 0.825 Å from samples, sealed in 0.3 mm diameter borosilicate glass capillaries. Neutron powder diffraction (NPD) data were collected using the POLARIS diffractometer at the ISIS neutron and muon source, from samples sealed under argon in 6 mm vanadium cans. Rietveld refinement were performed using the TOPAS suite of programs (v6).[30]

X-ray absorption experiments were performed at the B18 beamline of the Diamond Light Source. The measurements were carried out using the Pt-coated branch of the collimating and focusing mirrors, a Si(111) double-crystal monochromator and a pair of harmonic rejection mirrors. The size of the beam at the sample position was approximately 600 $\mu$m × 700 $\mu$m. X-ray absorption near-edge spectroscopy (XANES) data were collected at the Fe K-edge (7112 eV) in transmission mode with ion chambers before and behind the sample filled with appropriate mixtures of inert gases to optimize sensitivity ($I_0$: 300 mbar of $N_2$ and 700 mbar of He, resulting in an overall efficiency of 10%; $I_t$: 150 mbar of Ar and 850 mbar of He, with 70% efficiency). The spectra were measured with a step size equivalent to 0.25 eV and energy calibrated using metallic Fe foil. Data were normalized using the program Athena[31] with a linear pre-edge and polynomial postedge background subtracted from the raw $\ln(I_t/I_0)$ data. The samples were prepared in the form of a self-supported pellet, with the thickness optimized to obtain an edge jump close to 1.

Oxygen K-edge soft XAS and high-resolution Resonant inelastic X-ray scattering (RIXS) studies were performed on the I21 beamline[32] at the Diamond Light Source. Powder samples were ground together with graphite and pressed onto adhesive carbon tapes, which were then loaded onto sample pucks. The sample pucks were loaded into a vacuum suitcase in a glovebox and transported to the beamline. All measurements were performed at 20 K with continuous beam rastering under ultrahigh vacuum conditions. XAS data were obtained in total fluorescence (TFY) mode. The data were initially processed via a standardized procedure at the beamline. Further processing, i.e., background subtraction and normalization, were carried out using the Athena software.[31] In all cases, the XAS data presented are an average of multiple individual scans.

O K-edge RIXS maps were collected between excitation energies of 527.5 and 533 eV with steps of 0.25 eV for 60 s each. The beam was moved approximately 0.01 mm for every scan. Data calibration was performed by measuring a carbon tape after every spectrum. The raw data was processed using the Data Analysis WorkbeNch (DAWN)[33] software using established procedures at the beamline.

**Electrochemical Characterization.** The electrode material was formed from a mixture of active material, electronically conductive carbon black C-NERGY Super C65 (Imerys Graphite and Carbon, Belgium) and PVDF (polyvinylidene fluoride) (MTI Corporation, USA) as a binder, in a ratio of 8:1:1. The materials were ground using an Agate pestle and mortar for 15 min. A slurry was made by adding NMP (*N*-methyl-2-pyrrolidone) (Merck, Germany) and mixed using a Thinky ARE-250 mixer (Intertronics, UK). The slurry was cast on carbon coated aluminum foil using an MTI MSK-AFA-L800 tape caster (MTI Corporation, USA) and dried at 80 °C, before being transferred to an 80 °C vacuum oven for a minimum of 16 h. Cathodes were cut to 12 mm using an MTI disc cutter (MTI Corporation, USA). CR2032 SS316 coin cells were assembled using the cathodes, 16 mm separators cut from Whatman glass microfibre (GF/F grade) (Merck, Germany), and precut 15.6 mm lithium chips of 0.25 mm thickness (Cambridge Energy Solutions Ltd., UK) were used as the anode. The electrolyte was 1 M LiPF6 in ethylene carbonate and ethyl methyl carbonate 3:7 v/v (Solvionic, France). Cyclic voltammetry (CV) measurements were conducted using a Biologic VMP-300 potentiostat at room temperature and the galvanostatic cycling measurements were conducted using a MACCOR Series 4000 analyzer (Maccor, USA) at 25 °C.

Samples of $LiFe_{0.5}Al_{0.5}O_2$ were found to have extremely low conductivity. To improve this samples of $NaFe_{0.5}Al_{0.5}O_2$ were ball-milled prior to conversion to $LiFe_{0.5}Al_{0.5}O_2$, to enhance their conductivity, as ball-milling $LiFe_{0.5}Al_{0.5}O_2$ directly was found to lead to decomposition of the phase and the formation of $LiFe_5O_8$ as observed previously.[23]

## ■ RESULTS

**Structural Characterization of $NaFe_{1-x}M_xO_2$ and $LiFe_{1-x}M_xO_2$ (*M* = Al, Ga) Phases.** SXRD data collected from samples of $NaFe_{1-x}Al_xO_2$ ($x$ = 0.25, 0.5, 0.75) and $NaFe_{1-x}Ga_xO_2$ ($x$ = 0.1, 0.2, 0.3, 0.4, 0.5, 0.75) could be indexed using orthorhombic unit cells, exhibiting reflection conditions consistent with space group $Pna2_1$ (#33) in agreement with the reported structure of $\beta$-$NaFeO_2$.[34] Thus, structural models based on the structure of $\beta$-$NaFeO_2$ were constructed with the Fe cations replaced by Fe/M solid solutions, and these models were refined against the SXRD data to achieve good fits, as described in detail in the Supporting Information. Lattice parameters and unit cell volumes, plotted in Figure S11, show smooth changes as a function of composition, consistent with the formation of complete solid solutions. These data are in good agreement with previous reports of the $NaFe_{1-x}Al_xO_2$ series.[35]

SXRD data collected from samples of $LiFe_{1-x}Al_xO_2$ ($x$ = 0.25, 0.5, 0.75), prepared by cation exchange of the corresponding $NaFe_{1-x}Al_xO_2$ phases, could be indexed using orthorhombic unit cells, which are significantly contracted when compared to the cells of the corresponding $NaFe_{1-x}Al_xO_2$ phases. These data exhibit reflection conditions consistent with space group $Pna2_1$ (#33) and are consistent with the reported structure of T-$LiFeO_2$.[23] To locate the


https://doi.org/10.1021/acs.chemmater.4c03322
Chem. Mater. 2025, 37, 3171−3184

position of the lithium ions, NPD data were collected from a sample of $LiFe_{0.5}Al_{0.5}O_2$. The NPD data could also be indexed using an orthorhombic cell. A structural model based on the structure of $NaFe_{0.5}Al_{0.5}O_2$, but with Na replaced by Li, refined smoothly to give a good fit to the NPD data (Figure 2)

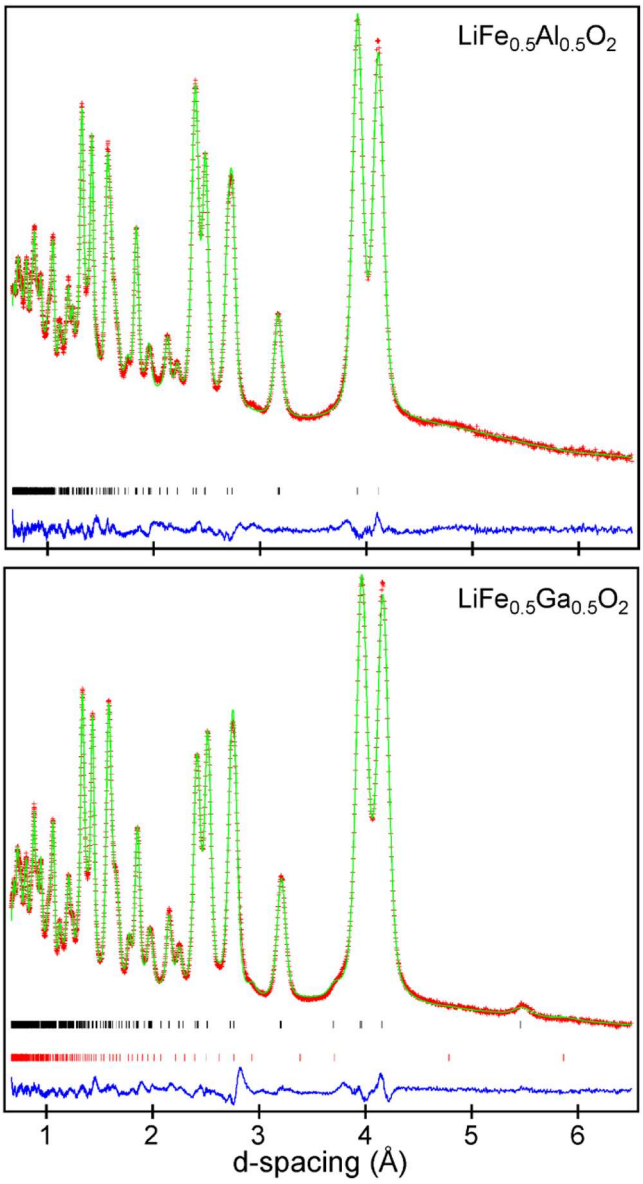


**Figure 2.** Observed calculated and difference plots from the structural refinement of $LiFe_{0.5}Al_{0.5}O_2$ (top) and $LiFe_{0.5}Ga_{0.5}O_2$ (bottom) against NPD data. Black tick marks indicate peak positions of the majority phase, red tick marks indicate peak positions of a secondary $LiFe_5O_8$ phases in the gallium-containing sample.

confirming that the lithium ions reside within the tetrahedral coordination sites previously occupied by Na, as described in the Table S12. Thus, structural models were constructed for the remaining $LiFe_{1-x}Al_xO_2$ phases with the lithium cations located and fixed at the positions previously occupied by Na in the corresponding $NaFe_{1-x}Al_xO_2$ phases. These models were refined against the SXRD data to achieve good fits, as described in detail in the Supporting Information.

SXRD data collected from samples of $LiFe_{1-x}Ga_xO_2$ ($x$ = 0.1, 0.2, 0.3, 0.4, 0.5, 0.75) could also be indexed using contracted orthorhombic unit cells with reflection conditions consistent with $Pna2_1$ space group symmetry. However, NPD data collected from a sample of $LiFe_{0.5}Ga_{0.5}O_2$ exhibited additional reflections inconsistent with $Pna2_1$ space group symmetry.

A symmetry analysis revealed the additional reflections are consistent with iron/gallium ordering in a manner analogous to the ordering of zinc and germanium in $Li_2ZnGeO_4$.[36] Thus, an Fe/Ga cation-ordered model was constructed (space group $Pn$) and refined against the NPD data to achieve a good fit (Figure 2) with structural details described in the Table S18 and a representation of the cation ordered structure shown in Figure 1.

Close inspection of the SXRD data collected from $LiFe_{0.5}Ga_{0.5}O_2$ show no reflections that cannot be indexed by the orthorhombic $Pna2_1$ cell. In addition, structural refinement of cation-disordered orthorhombic ($Pna2_1$) and cation-ordered monoclinic ($Pn$) models give equivalently good fits to the SXRD data. We therefore conclude that SXRD is insensitive to Fe/Ga ordering, so a series of Fe/Ga cation-disordered structural models were constructed for the remaining $LiFe_{1-x}Ga_xO_2$ phases and these were refined against the SXRD data collected from these materials, to achieve good fits as described in the Supporting Information. As the SXRD data are insensitive to Fe/Ga order, it is not possible for us to be sure if other $LiFe_{1-x}Ga_xO_2$ phases are cation ordered (we were unable to collect NPD data from these phases). However, given the strong cation order observed in $LiFe_{0.5}Ga_{0.5}O_2$ we think it is likely that $LiFe_{1-x}Ga_xO_2$ phases with $x \sim 0.5$ will also exhibit a degree of cation ordering. Lattice parameters and unit cell volumes of the $LiFe_{1-x}M_xO_2$ phases, plotted in Figure S21, show smooth changes as a function of composition, consistent with the formation of complete solid solutions.

**Chemical Lithiation of $LiFe_{1-x}M_xO_2$ ($M$ = Al, Ga) Phases.** SXRD data collected from samples of T-$LiFeO_2$ reacted with $n$-BuLi as described above, reveal the majority of the sample has been converted to elemental Fe, with only small quantities of poorly crystalline T-$LiFeO_2$ remaining, indicating this phase cannot be topochemically reduced by lithium insertion under these conditions. Exposure to $n$-BuLi also led to the decomposition of all of the $LiFe_{1-x}Al_xO_2$ phases, with elemental Fe and poorly crystalline $LiFe_{1-x}Al_xO_2$ being the only products observed.

However, SXRD data collected from $LiFe_{1-x}Ga_xO_2$ samples treated with $n$-BuLi exhibited sharp diffraction peaks which could be indexed using orthorhombic unit cells with lattice parameters very similar to those of the "pristine" $LiFe_{1-x}Ga_xO_2$ parent phases. Refinement of the corresponding $LiFe_{1-x}Ga_xO_2$ structural models against the SXRD data achieved good fits and revealed the $x$ = 0.1, 0.2, and 0.3 samples contained ~ 8 wt % elemental Fe, with no sign of Fe in any of the remaining compositions, as detailed in the Supporting Information. Due to the low X-ray scattering power of lithium, the Li site position was not allowed to vary and no account was taken of any additional lithium inserted within the structural models during the structural refinements.

To better understand the crystal structure of the lithiated $Li_{1+\delta}Fe_{1-x}Ga_xO_2$ phases, NPD data were collected from a sample of $Li_{1+\delta}Fe_{0.5}Ga_{0.5}O_2$. These data could be indexed using a monoclinic cell of similar dimensions to that of unlithiated $LiFe_{0.5}Ga_{0.5}O_2$, so a structural model based on the Fe/Ga cation ordered structure of $Li_1Fe_{0.5}Ga_{0.5}O_2$ was refined against the data to achieve a reasonable fit. A Fourier difference map


https://doi.org/10.1021/acs.chemmater.4c03322
Chem. Mater. 2025, 37, 3171−3184

was calculated at this stage to locate the positions of the inserted lithium ions. This map revealed 4 strong negative minima within the unit cell (neutron scattering length of Li = −1.90 fm)[37] located within vacant octahedral coordination sites as shown in Figure 3, so lithium ions were inserted into

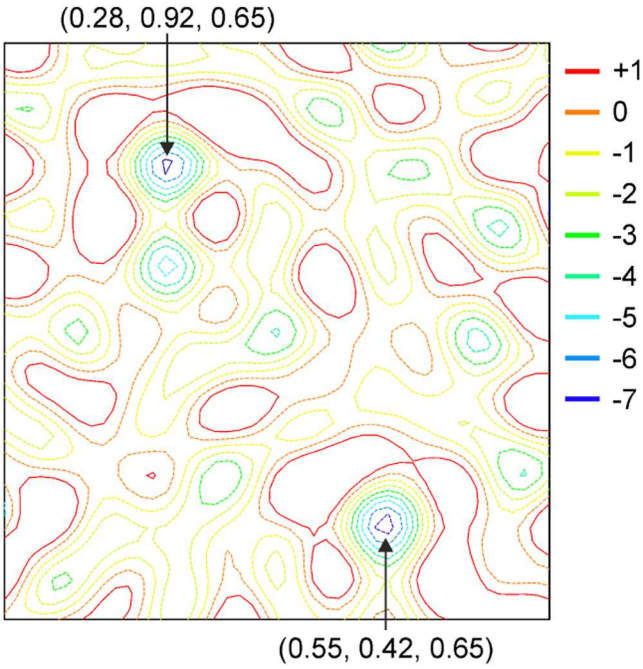


**Figure 3.** Plot of $z$ = 0.65 plane of the Fourier difference map calculated to located the additional lithium locations in $Li_{1.47}Fe_{0.5}Ga_{0.5}O_2$. Negative minima indicated reside within empty octahedral coordination sites within the Li−Fe−Ga-O framework.

the model at these sites and their positions and occupancies refined to yield a phase of overall composition $Li_{1.47(2)}Fe_{0.5}Ga_{0.5}O_2$ consistent with the composition of $Li_{1.47(4)}Fe_{0.5}Ga_{0.5}O_2$ determined by iodometric titration. Close inspection of the NPD data revealed a series of weak reflections consistent with 9 wt % $LiFe_5O_8$ in the sample. This was added to the structural model, which converged to give a good fit to the data as shown in Figure 4a and detailed in Table S24.

Fe K-edge XANES data collected from $LiFe_{0.5}Ga_{0.5}O_2$ and $Li_{1.5}Fe_{0.5}Ga_{0.5}O_2$ are shown in Figure 4b. Both spectra exhibit a strong pre-edge feature at ∼ 7112 eV, consistent with the tetrahedral coordination of iron, and the absorption edge of $Li_{1.5}Fe_{0.5}Ga_{0.5}O_2$ is observed at lower energy than the absorption edge of pristine $LiFe_{0.5}Ga_{0.5}O_2$, consistent with the reduction of $Fe^{3+}$ to $Fe^{2+}$ on lithium insertion.

**Chemical Delithiation of $LiFe_{1-x}Al_xO_2$ Phases.** SXRD data collected from a sample of T-$LiFeO_2$ treated with $NO_2BF_4$, as described above, exhibit very broad diffraction features, indicating structural decomposition has occurred. SXRD data collected after this sample was annealed in an evacuated silica ampule at 600 °C indicate the presence of the spinel $LiFe_5O_8$, consistent with previous reports describing the electrochemical delithiation of T-$LiFeO_2$.[23]

SXRD data collected from oxidized $Li_{1-\delta}Fe_{1-x}Al_xO_2$ samples with $x$ > 0.25 exhibit sharp diffraction peaks which could be indexed by orthorhombic unit cells similar to the corresponding $Li_{1.0}Fe_{1-x}Al_xO_2$ phases. Structural models based on the pristine $LiFe_{1-x}Al_xO_2$ materials were refined against these

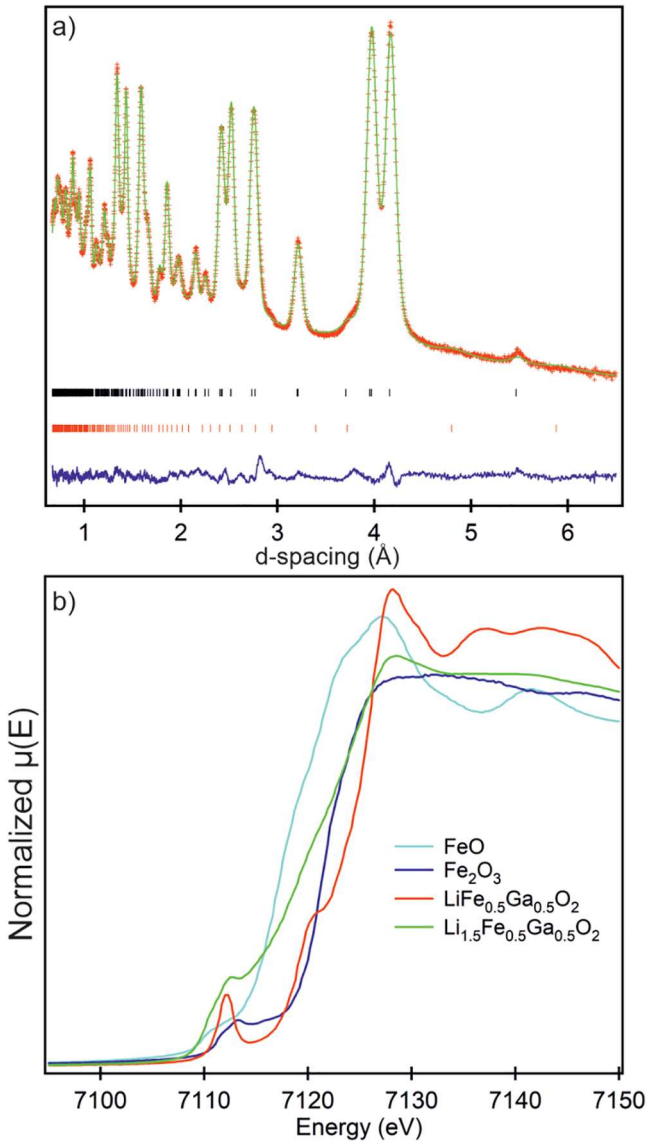


**Figure 4.** (a) Observed, calculated and difference plots from the structural refinement of $Li_{1.5}Fe_{0.5}Ga_{0.5}O_2$ against NPD data collected at room temperature. Black tick marks indicate peak positions of $Li_{1.5}Fe_{0.5}Ga_{0.5}O_2$, red tick marks $LiFe_5O_8$. (b) XANES data from the Fe K-edges of $LiFe_{0.5}Ga_{0.5}O_2$, $Li_{1.5}Fe_{0.5}Ga_{0.5}O_2$, with data from FeO and $Fe_2O_3$ acting as standards for $Fe^{2+}$ and $Fe^{3+}$ respectively.

SXRD data to achieve good fits. Again, due to the low X-ray scattering power of lithium no attempt was made to refine the position or occupancy of the lithium cation sites.

NPD data collected from an oxidized sample of $LiFe_{0.5}Al_{0.5}O_2$ could be indexed using the unit cell of the pristine material and fit well by a structural model based on $LiFe_{0.5}Al_{0.5}O_2$ in which the position and occupancy of the Li site was allowed to vary. The refinement converged to give a model with composition $Li_{0.80(1)}Fe_{0.5}Al_{0.5}O_2$ which is in good agreement with ICP-MS data. Full details of the refined structure are given in Table S28 with a plot of the data shown in Figure 5a. Reaction with LiI, as described above, indicate that 0.08 Li per formula unit can be chemically reinserted into $Li_{0.8}Fe_{0.5}Al_{0.5}O_2$.

Previous studies of the T-$LiFeO_2$ system suggest proton-for-lithium exchange can occur on delithiation.[23] The presence of protons within $Li_{1-\delta}Fe_{0.5}Al_{0.5}O_2$ would result in a large


https://doi.org/10.1021/acs.chemmater.4c03322
Chem. Mater. 2025, 37, 3171−3184

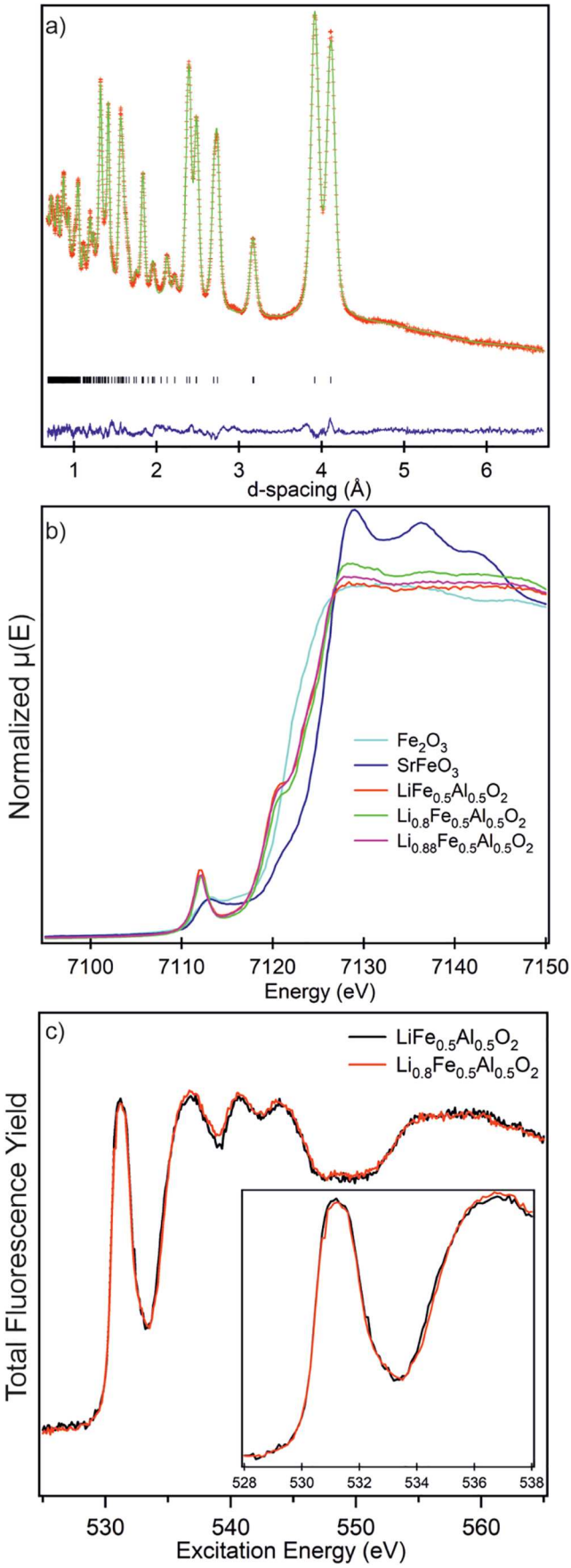


**Figure 5.** (a) Observed, calculated and difference plots from the structural refinement of $Li_{0.8}Fe_{0.5}Al_{0.5}O_2$ against NPD data collected at room temperature. (b) XANES data from the Fe K-edges of $LiFe_{0.5}Al_{0.5}O_2$, $Li_{0.8}Fe_{0.5}Al_{0.5}O_2$ and $Li_{0.88}Fe_{0.5}Al_{0.5}O_2$ with data from $Fe_2O_3$ and $SrFeO_3$ acting as standards for $Fe^{3+}$ and $Fe^{4+}$ respectively. (c) Oxygen k-edge XAS data collected from $LiFe_{0.5}Al_{0.5}O_2$ and $Li_{0.8}Fe_{0.5}Al_{0.5}O_2$ in fluorescence mode.

incoherent and inelastic background in the NPD data collected from this phase, which is not observed (Figure 5a, S30).

Fe K-edge XANES data collected from $LiFe_{0.5}Al_{0.5}O_2$, $Li_{0.8}Fe_{0.5}Al_{0.5}O_2$ and $Li_{0.88}Fe_{0.5}Al_{0.5}O_2$ (prepared by reaction between $Li_{0.8}Fe_{0.5}Al_{0.5}O_2$ and LiI) are shown in Figure 5b along with spectra from $Fe_2O_3$ and $SrFeO_3$ to act as $Fe^{3+}$ and $Fe^{4+}$ standards, respectively.

The spectra from the $Li_yFe_{0.5}Al_{0.5}O_2$ phases all exhibit a strong pre-edge feature at ∼ 7112 eV, consistent with the tetrahedral coordination of Fe. However, the absorption edge positions of the normalized spectra from the 3 $Li_yFe_{0.5}Al_{0.5}O_2$ phases are almost identical, which is surprising given that expected average Fe oxidation states for $LiFe_{0.5}Al_{0.5}O_2$, $Li_{0.8}Fe_{0.5}Al_{0.5}O_2$ and $Li_{0.88}Fe_{0.5}Al_{0.5}O_2$ are $Fe^{3+}$, $Fe^{3.4+}$ and $Fe^{3.24+}$ respectively. This suggests that the removal of lithium from $LiFe_{0.5}Al_{0.5}O_2$ does not simply oxidize $Fe^{3+}$ cations to $Fe^{4+}$.

To further investigate the nature of the oxidized $Li_{1-\delta}Fe_{0.5}Al_{0.5}O_2$ materials, oxygen K-edge X-ray absorption data were collected in fluorescence yield mode from pristine $LiFe_{0.5}Al_{0.5}O_2$ and oxidized $Li_{0.8}Fe_{0.5}Al_{0.5}O_2$, as shown in Figure 5c. The data exhibit two features: a lower energy feature with a local maximum at ∼ 531 eV and a higher energy feature with a maximum at ∼ 536 eV which are attributed to the excitation of oxygen 1*s* electrons to the empty states in the Fe(3*d*)-O(2*p*) and Fe(4*s*, 4*p*)-O(2*p*) hybridized bands, respectively.[38] Comparison of the fluorescence-yield data from the two samples reveals no change to the absorption edge position of the Fe(3*d*)-O(2*p*) excitation feature and a small shift to higher energy of the Fe(4*s*, 4*p*)-O(2*p*) feature on oxidation of $LiFe_{0.5}Al_{0.5}O_2$.

Oxygen K-edge resonant inelastic X-ray scattering (RIXS) data collected from pristine $LiFe_{0.5}Al_{0.5}O_2$ and oxidized $Li_{0.8}Fe_{0.5}Al_{0.5}O_2$ are plotted in Figures 6a,b, respectively. The data collected from pristine $LiFe_{0.5}Al_{0.5}O_2$ exhibit an emission feature in the range 524 − 527 eV excited by energies in the range 530 − 533 eV, which by comparison to the O-XAS data in Figure 5c, can be attributed to the excitation of an O 1s electron into empty Fe(3d)−O(2p) hybridized states and the subsequent relaxation of an electron from the filled O(2p) band to refill the O(1s) hole. RIXS data collected from $Li_{0.8}Fe_{0.5}Al_{0.5}O_2$ exhibit the same feature, but reveal it extends to an additional future at an excitation energy of ∼ 531.75 eV and emission energy ∼ 523.5 eV (marked with an arrow in Figure 6b), which can be clearly seen in the partial integrated fluorescence yields of the two data sets, shown in Figure 6c. The individual RIXS line-scans collected at excitation energies in the range 531.25 − 531.75 eV from $LiFe_{0.5}Al_{0.5}O_2$ and $Li_{0.8}Fe_{0.5}Al_{0.5}O_2$ (plotted in Figure S36) also exhibit this additional feature in the data from the oxidized sample. Enhanced emission signals at this combination of excitation and emission energy are widely seen in RIXS data collected from cathode materials exhibiting "anion redox" in their charged states.[39−42] We therefore attribute this additional


https://doi.org/10.1021/acs.chemmater.4c03322
Chem. Mater. 2025, 37, 3171−3184

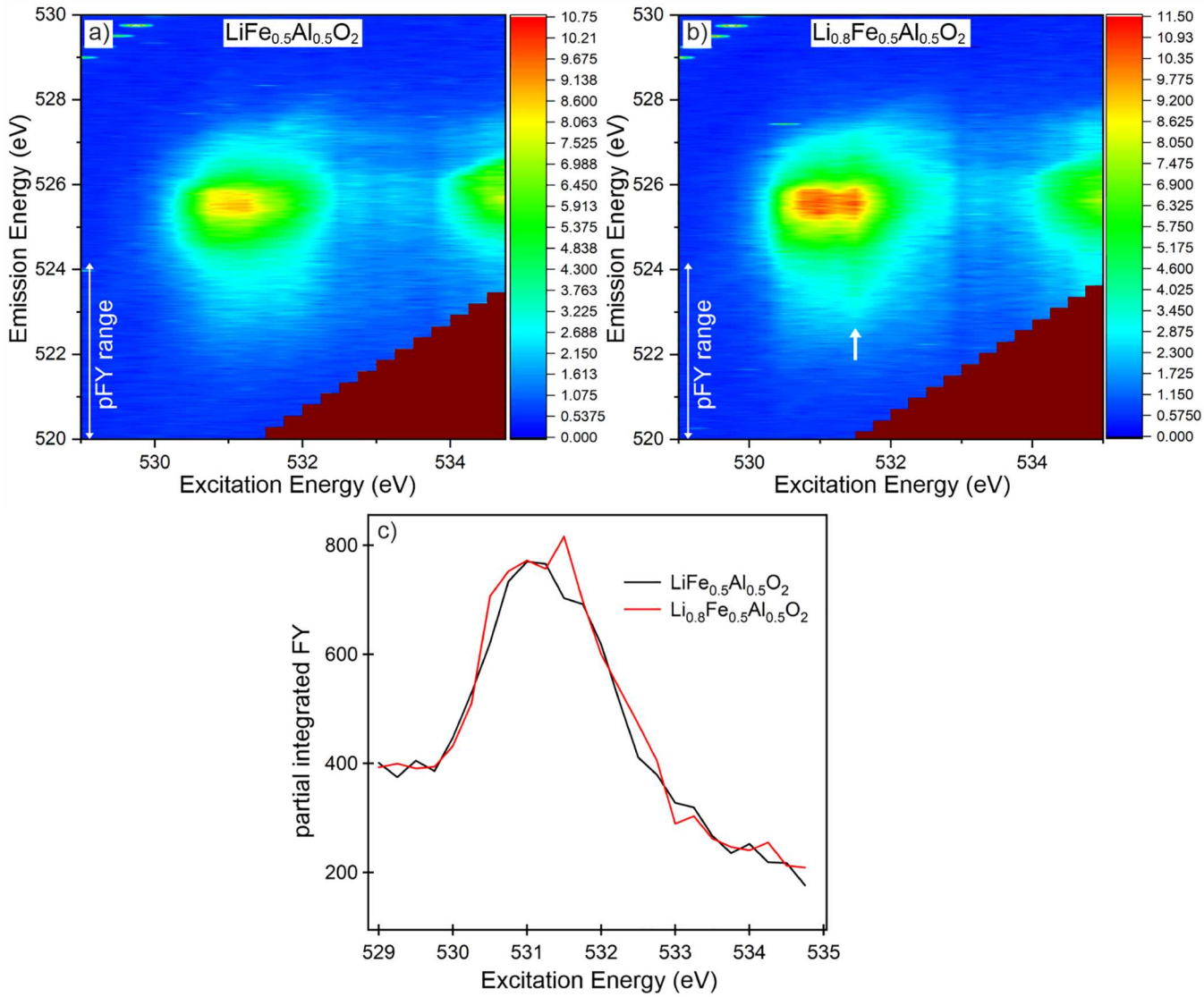


**Figure 6.** RIXS data collected from a) $LiFe_{0.5}Al_{0.5}O_2$ and b) $Li_{0.8}Fe_{0.5}Al_{0.5}O_2$. c) partial fluorescence yields of $LiFe_{0.5}Al_{0.5}O_2$ and $Li_{0.8}Fe_{0.5}Al_{0.5}O_2$ integrated over the emission energy range 520 − 524.25 eV.

RIXS signal to the participation of oxygen in the redox chemistry of the system on lithium extraction.

Systems exhibiting anion participation in their redox chemistry can be organized into two groups: (i) those in which the "anion hole" is localized within $O_2^{n-}$ peroxide or superoxide species,[9,43−45] and (ii) those in which the generation of anion holes does not lead to the formation of molecular anions.[46−49] Systems in the former group tend to exhibit distinct features in XPS and soft O-XAS spectra associated with the $O_2^{n-}$ molecular anions,[9,45] which are absent from the data collected from $Li_{0.8}Fe_{0.5}Al_{0.5}O_2$. We therefore assign the $Li_{1-x}Fe_{0.5}Al_{0.5}O_2$ system to the second grouping − those without $O_2^{n-}$ molecular anions.

We also note that spectroscopic studies of oxides such as $SrFeO_3$, which nominally contain $Fe^{4+}$, exhibit evidence for strong hybridization between Fe(3d) and O(2p) states, so that the electronic ground state is considered to be a mixture of $3d^4$ and $3d^5\underline{L}$ configurations (where $\underline{L}$ indicates a localized ligand hole).[7,50−52] Such a scenario appears to fit our observations well (no shift in Fe XANES on oxidation; indication from RIXS data of oxygen redox participation; no indication of $O_2^{n-}$ formation), we therefore propose that on lithium extraction electrons are removed from strongly hybridized Fe(3d)-O(2p) states to leave localized holes, analogous to the $3d^5\underline{L}$ states described above, which we will refer to as $Fe^{IV}$−O centers, as discussed in more detail below.

**Chemical Delithiation of $LiFe_{1-x}Ga_xO_2$ Phases.** SXRD data collected from $LiFe_{1-x}Ga_xO_2$ ($0 < x < 0.4$) phases reacted with $NO_2BF_4$ as described above, exhibit no sharp diffraction features, indicating these phases decompose under these oxidizing conditions, in common with undoped $LiFeO_2$, as shown in the Supporting Information. However, SXRD data collected from oxidized samples of $LiFe_{0.5}Ga_{0.5}O_2$ and $LiFe_{0.25}Ga_{0.75}O_2$ can be indexed using orthorhombic unit cells and fit using structural models based on the corresponding $Li_{1.0}Fe_{1-x}Ga_xO_2$ phases. NPD data collected from $Li_{1-\delta}Fe_{0.5}Ga_{0.5}O_2$ could be fit using a Fe/Ga cation ordered model. Refinement of the lithium cation positions and occupancies yielded a model of composition $Li_{0.60(2)}Fe_{0.5}Ga_{0.5}O_2$ in good agreement with a composition of $Li_{0.57}Fe_{0.5}Ga_{0.5}O_2$ determined by ICP-MS. Full details of the refined structure are given in Table S30 with a plot of the data


https://doi.org/10.1021/acs.chemmater.4c03322
Chem. Mater. 2025, 37, 3171−3184

shown in Figure 7a. Reaction with LiI, as described above, indicates 0.13 Li per formula unit can be chemically reinserted into $Li_{0.60}Fe_{0.5}Ga_{0.5}O_2$.

Fe K-edge XANES data collected from $LiFe_{0.5}Ga_{0.5}O_2$, $Li_{0.60}Fe_{0.5}Ga_{0.5}O_2$ and $Li_{0.73}Fe_{0.5}Ga_{0.5}O_2$ (prepared by reaction between $Li_{0.60}Fe_{0.5}Ga_{0.5}O_2$ and LiI) are shown in Figure 7b, along with $Fe^{3+}$ and $Fe^{4+}$ standard spectra. In common with the Fe/Al phases, these spectra show a strong pre-edge feature at ∼ 7112 eV consistent with the tetrahedral coordination of Fe. Again, in common with the $Li_yFe_{0.5}Al_{0.5}O_2$ phases, the absorption edges of the three $Li_yFe_{0.5}Ga_{0.5}O_2$ phases are almost identical despite the expected average Fe oxidation states for $LiFe_{0.5}Ga_{0.5}O_2$, $Li_{0.57}Fe_{0.5}Ga_{0.5}O_2$ and $Li_{0.73}Fe_{0.5}Ga_{0.5}O_2$ being $Fe^{3+}$, $Fe^{3.8+}$ and $Fe^{3.54+}$ respectively. Again, this indicates the removal of lithium from $LiFe_{0.5}Ga_{0.5}O_2$ does not simply oxidize $Fe^{3+}$ to $Fe^{4+}$.

Oxygen K-edge X-ray absorption data collected in fluorescence yield mode from pristine $LiFe_{0.5}Ga_{0.5}O_2$ and oxidized $Li_{0.6}Fe_{0.5}Ga_{0.5}O_2$, shown in Figure 7c. Again the data exhibit a lower energy feature with a local maximum at ∼ 531 eV attributed to the excitation of oxygen 1*s* electrons to the empty states in the Fe(3*d*)-O(2*p*) hybridized band, and a higher energy feature with a maximum at ∼ 536 eV attributed to the excitation of oxygen 1*s* electrons to the empty states in the Fe(4*s*, 4*p*)-O(2*p*) hybridized band.[38] Comparison of the fluorescence-yield data from the two samples reveals no change to the absorption edge position of the Fe(3*d*)-O(2*p*) excitation feature, but a small decline in intensity, and a small shift to higher energy of the Fe(4*s*, 4*p*)-O(2*p*) feature on oxidation of $LiFe_{0.5}Ga_{0.5}O_2$.

**Electrochemical Characterization.** CV data collected from $LiFe_{0.5}Al_{0.5}O_2$ in the range 2.5−4.8 V (Figure 8b) show two separate redox processes. On sweeping the potential up from 2.6 V there is an oxidation which occurs above 4 V which does not appear to have a corresponding reduction process, and which declines in magnitude on repeated voltage cycling. This can be seen more clearly in analogous CV data collected from $LiFe_{0.5}Al_{0.5}O_2$ between 3 and 4.8 V, shown in Figure 8a. We attribute this irreversible feature to the oxidation of $Fe^{III}$ to form $Fe^{IV}$−O "anion redox" centers seen in the chemical oxidation of $LiFe_{0.5}Al_{0.5}O_2$. On sweeping the potential below 3.25 V a reduction occurs which has a corresponding oxidation feature between 2.5 and 3 V. We attribute this reversible, low-potential feature to the reversible reduction of $Fe^{III}$ to $Fe^{II}$ on lithium (re)insertion. It was not possible to collect electrochemical data from $LiFe_{0.5}Al_{0.5}O_2$ at potentials below 2.5 V without the sample decomposing by extrusion of elemental iron, in agreement with the observed instability of $LiFe_{1-x}Al_xO_2$ phases on exposure to *n*-BuLi.

CV data collected from $LiFe_{0.5}Ga_{0.5}O_2$ in the range 2 − 4.8 V (Figure 8d) are qualitatively similar to those of $LiFe_{0.5}Al_{0.5}O_2$ exhibiting a high potential (E > 3.75 V) irreversible oxidation which declines in magnitude on voltage cycling, and a low-potential (E < 3.75 V) reversible feature, shown more clearly in analogous CV data collected between 1.9 and 4 V (Figure 8c).

Again, these features are attributed to the irreversible formation of $Fe^{IV}$−O centers at high potential and the reversible cycling of $Fe^{III}$ to $Fe^{II}$ at low potential.

Capacity data collected during charge−discharge cycling of $LiFe_{0.5}Ga_{0.5}O_2$ in the range 1 − 4.8 V (Figure 9a) clearly exhibit the same redox processes observed in the CV data − an irreversible oxidation above 3.75 V and a reversible redox

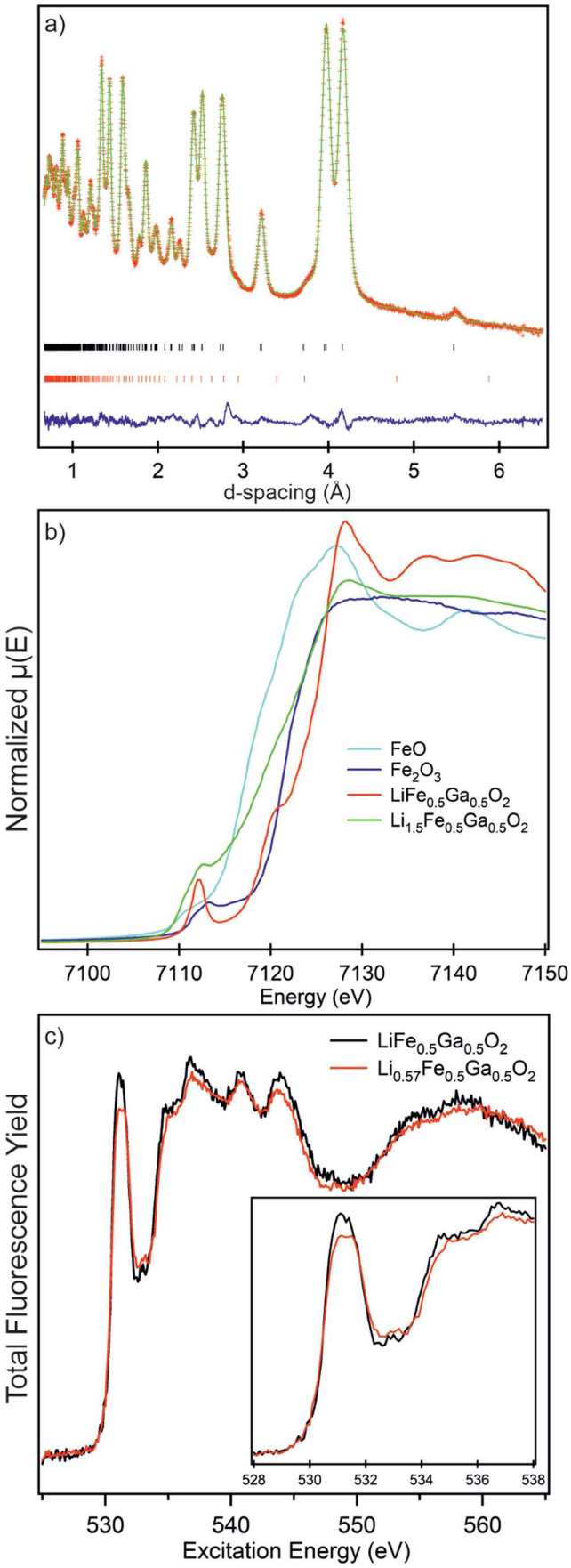


**Figure 7.** (a) Observed, calculated and difference plots from the structural refinement of $Li_{1-\delta}Fe_{0.5}Ga_{0.5}O_2$ against NPD data collected


https://doi.org/10.1021/acs.chemmater.4c03322
Chem. Mater. 2025, 37, 3171−3184

**Figure** 7. continued

at room temperature. (b) XANES data from the Fe K-edges of $LiFe_{0.5}Ga_{0.5}O_2$, $Li_{0.60}Fe_{0.5}Ga_{0.5}O_2$ and $Li_{0.73}Fe_{0.5}Ga_{0.5}O_2$ with data from $Fe_2O_3$ and $SrFeO_3$ acting as standards for $Fe^{3+}$ and $Fe^{4+}$ respectively. (c) Oxygen K-edge XAS data collected from $LiFe_{0.5}Ga_{0.5}O_2$ and $Li_{0.60}Fe_{0.5}Ga_{0.5}O_2$ in fluorescence mode.

process below 3 V. The compositional changes which occur on redox cycling can be seen more clearly in Figures 9b,d and e. In the first charge cycle, 0.05 Li per fu is extracted above 4 V, resulting in a cathode composition of $Li_{0.95}Fe_{0.5}Ga_{0.5}O_2$ as shown in Figure 9b,d, and as a consequence 10% of the Fe centers are oxidized to $Fe^{IV}$−O species (Figure 9e) so that the cathode composition can be written as $Li_{0.95}(Fe^{IV}–O)_{0.05}Fe^{III}_{0.45}Ga_{0.5}O_2$.

In the subsequent discharge cycle 0.31 Li per fu is inserted into the cathode at potentials below 3 V, to yield a sample of composition $Li_{1.26}Fe_{0.5}Ga_{0.5}O_2$. However, given the irreversible nature of the high-potential redox process, the insertion of lithium reduces the $Fe^{III}$ centers in the cathode, not the $Fe^{IV}$–O species, so the composition can be written as $Li_{1.26}(Fe^{IV}–O)_{0.05}Fe^{III}_{0.14}Fe^{II}_{0.31}Ga_{0.5}O_2$.

The second charge cycle removes 0.25 Li per fu from the cathode, which can be crudely partitioned between the low-potential redox process (Li extracted below 3.75 V) which oxidizes $Fe^{II}$ to $Fe^{III}$, and the high-potential redox process (Li extracted above 3.75 V) which oxidizes $Fe^{III}$ to $Fe^{IV}$−O (Figure 9e). Thus, at the end of the second charge cycle the cathode composition can be written as $Li_{1.01}(Fe^{IV}–O)_{0.075}Fe^{III}_{0.34}Fe^{II}_{0.085}Ga_{0.5}O_2$. This is then converted to

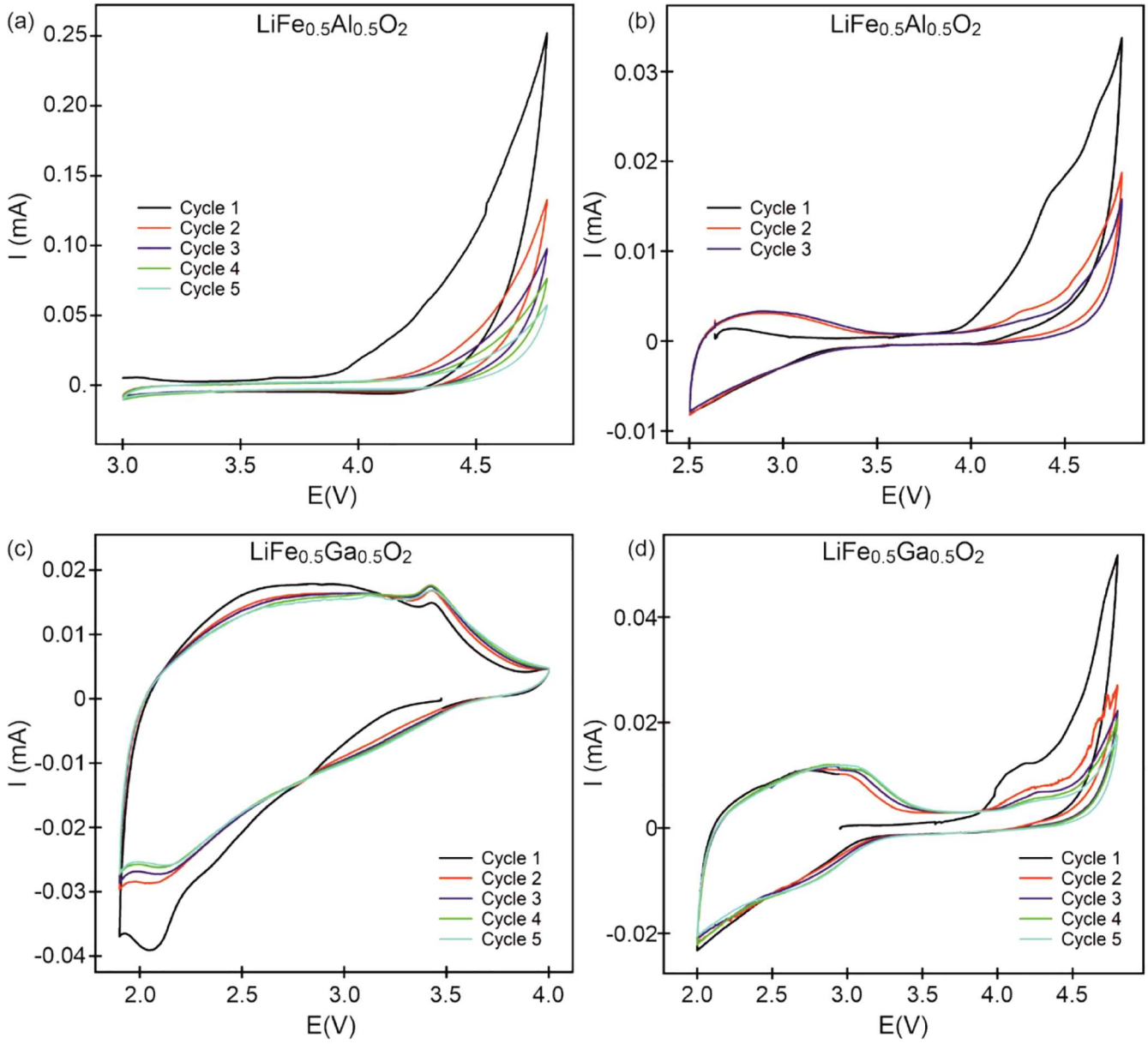


**Figure 8.** CV data collected from $LiFe_{0.5}Al_{0.5}O_2$ between (a) 3 and 4.8 V and (b) 2.5 and 4.8 V vs $Li^+$/Li. CV data collected from $LiFe_{0.5}Ga_{0.5}O_2$ between (a) 1.9 and 4 V and (b) 2.0 and 4.8 V vs $Li^+$/Li.


https://doi.org/10.1021/acs.chemmater.4c03322
Chem. Mater. 2025, 37, 3171−3184

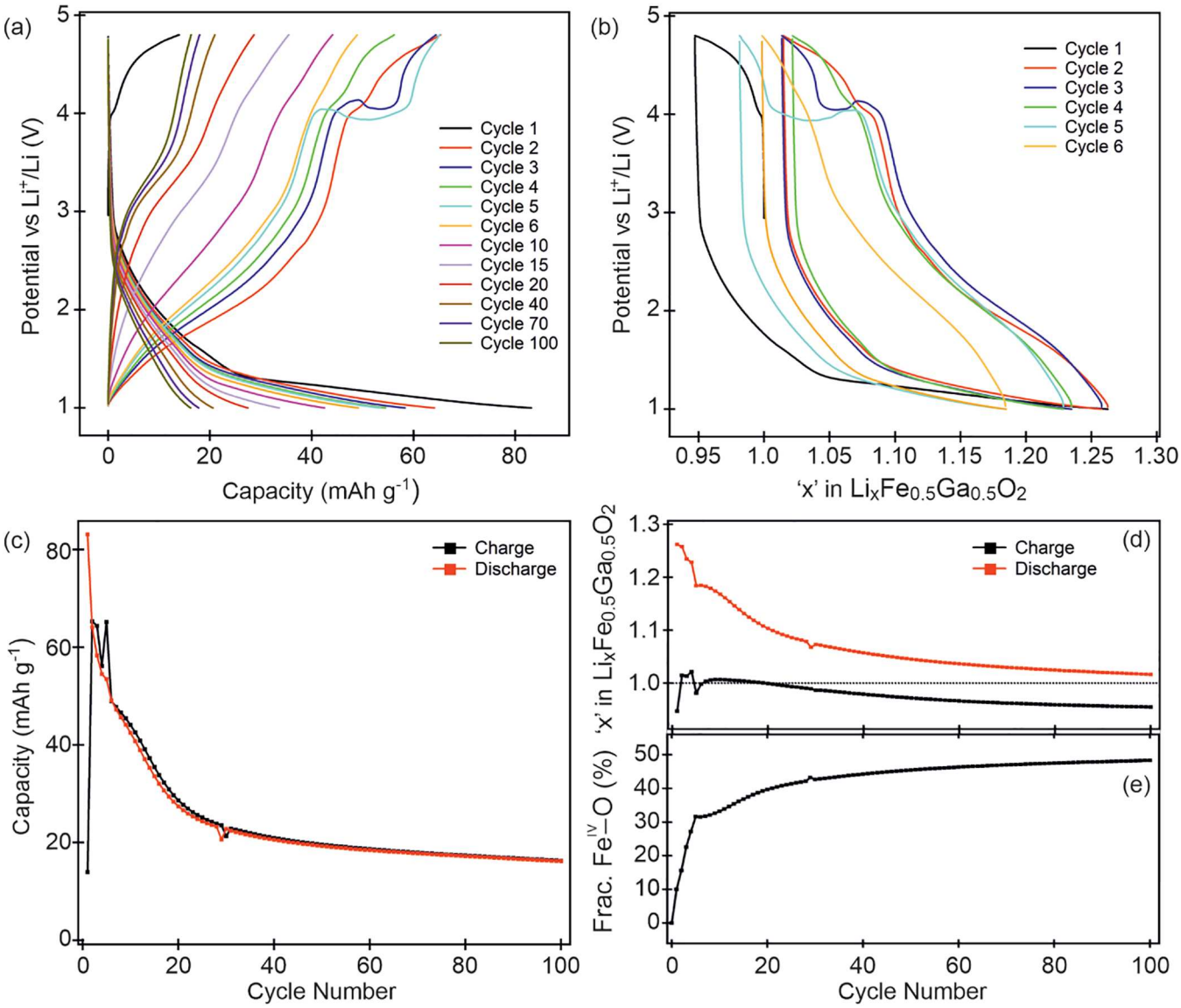


**Figure 9.** (a) Charge−discharge profiles of $LiFe_{0.5}Ga_{0.5}O_2$ in the range 1 − 4.8 V and (b) the accompanying compositional changes. (c) Plot of charge and discharge capacities as a function of cycle number, (d) the corresponding cathode lithium content at full charge and discharge and (e) the fraction of $Fe^{IV}$−O centers in the cathode.

$Li_{1.25}(Fe^{IV}–O)_{0.075}Fe^{III}_{0.10}Fe^{II}_{0.325}Ga_{0.5}O_2$ in the insertion of 0.24 Li per fu in the second discharge cycle.

This analysis shows that the irreversible nature of the high-potential redox process leads to the accumulation of $Fe^{IV}$−O centers and the depletion of $Fe^{3+}$ centers within the cathode on repeated cycling. Figure 9e shows that the concentration of $Fe^{IV}$−O continues to increase rapidly up to the fifth cycle, during which the fully charged state has a composition of $Li_{0.99}(Fe^{IV}–O)_{0.16}Fe^{III}_{0.19}Fe^{II}_{0.15}Ga_{0.5}O_2$ and crucially the fully discharged state has a composition of $Li_{1.18}(Fe^{IV}–O)_{0.16}Fe^{II}_{0.34}Ga_{0.5}O_2$ in which there appear to be no remaining $Fe^{III}$ centers.

The lack of $Fe^{III}$ centers in the cathode after the fifth discharge suggests that the discharge capacity in this and subsequent cycles is limited by the number of reducible $Fe^{III}$ centers present in the material (we preclude the reduction of $Fe^{II}$ to $Fe^{I}$ in our analysis) − a situation that was not true in the first 4 discharge cycles. Furthermore, it can be seen in Figures 9a,b that the high-potential part of the sixth charge cycle differs markedly from the fifth charge cycle, and shows that much less $Fe^{III}$ is converted to $Fe^{IV}$−O after the fifth cycle, suggesting that the low concentration of $Fe^{III}$ after the fifth discharge affects the high-potential redox process as well as the low-potential process.

In line with the analysis above, the data in Figure 9 show a qualitative change in charge/discharge behavior of the Li−Fe−Ga-O system after the fifth cycle. The lack of $Fe^{III}$ centers in the fully discharged state means that the cathode composition at full discharge can now be written as $Li_{1.5-2y}(Fe^{IV}–O)_yFe^{II}_{0.5-y}Ga_{0.5}O_2$. Thus, as the concentration of $Fe^{IV}$−O centers continues to rise between cycles 4 and 40 (increase in y, Figure 9e) the lithium content of the cathode in the fully discharged state declines (Figure 9d) as does the total discharge capacity (Figure 9c). After 40 cycles the total capacity appears to stabilize at around 20 $mAhg^{-1}$ (0.07 Li per fu) with the cathode composition being $Li_{0.98}(Fe^{IV}–O)_{0.225}Fe^{III}_{0.07}Fe^{II}_{0.205}Ga_{0.5}O_2$ at full charge, and $Li_{1.05}(Fe^{IV}–O)_{0.225}Fe^{II}_{0.275}Ga_{0.5}O_2$ at full discharge.


https://doi.org/10.1021/acs.chemmater.4c03322
Chem. Mater. 2025, 37, 3171−3184

Capacity data collected during charge−discharge cycling of $LiFe_{0.5}Al_{0.5}O_2$ in the range 2 − 4.8 V (Figure 10) also exhibit

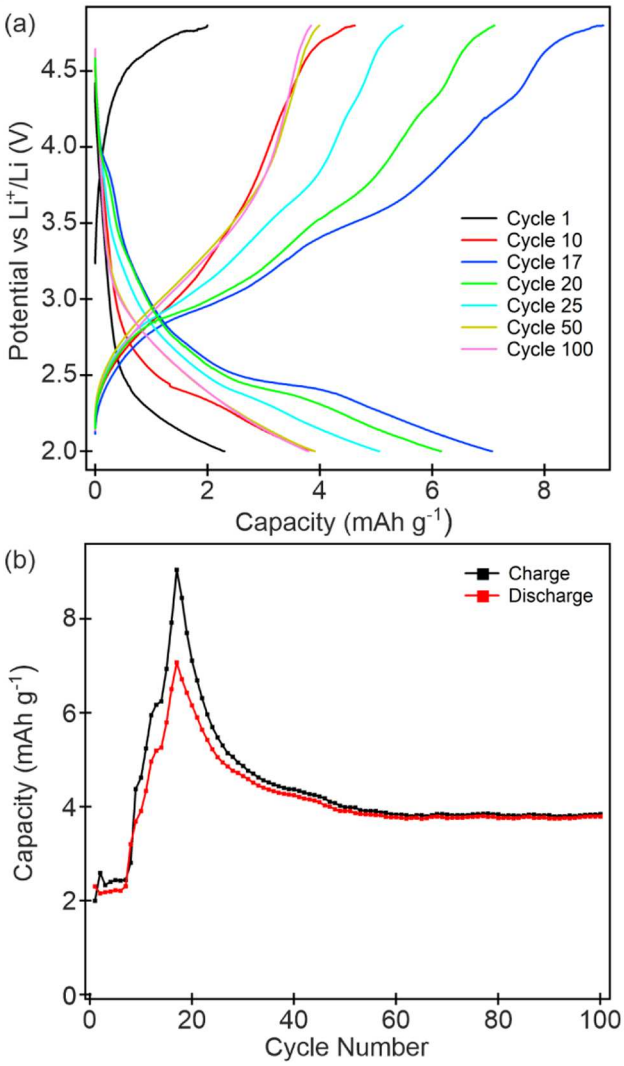


**Figure 10.** (a) Charge−discharge profiles of $LiFe_{0.5}Al_{0.5}O_2$ in the range 2 − 4.8 V (b) plot of corresponding charge and discharge capacities as a function of cycle.

two separate redox processes, in line with the CV data shown in Figure 8. However, the observed charge and discharge capacities are very small. This is attributed to two factors. First, the electrical resistivity of $LiFe_{0.5}Al_{0.5}O_2$ is very high − a feature also observed in other $LiFeO_2$ polymorphs.[19,20] This high electrical resistivity effect is relieved slightly on repeated cycling, as shown in Figure 10b. The second cause of the low capacity observed in the $LiFe_{0.5}Al_{0.5}O_2$ system is the instability of the material at low potentials, which necessitates the use of a narrow potential range (2 − 4.8 V) which is not sufficiently low to effectively cycle the $Fe^{III}$−$Fe^{II}$ redox process. However, within these restrictions, the data in Figure 10 show a significantly larger charge capacity than discharge capacity, consistent with the accumulation of $Fe^{IV}$−O centers, as described above for $LiFe_{0.5}Ga_{0.5}O_2$. However, the concentration of $Fe^{IV}$−O in the $LiFe_{0.5}Al_{0.5}O_2$ cycling regime never rises to a level where it significantly restricts the concentration of $Fe^{III}$ and thus the discharge capacity.

## ■ DISCUSSION

Replacing the $Fe^{3+}$ cations in $NaFeO_2$ with $Al^{3+}$ or $Ga^{3+}$ leads to a decline in the unit cell volume and an associated contraction in the average (Fe/M)−O bond length (Tables S32 and S33) in line with the 4-coordinate radii of the ions ($Fe^{3+}$ = 0.63 Å; $Al^{3+}$ = 0.53 Å; $Ga^{3+}$ = 0.61 Å)[12] Subsequent topochemical Li-for-Na cation exchange further contracts the unit cells of the $LiFe_{1-x}M_xO_2$ phases, but leads to an expansion of the average Fe−O bond length, as detailed in Tables S32 and S33. Previous studies of Fe-based cathode materials have shown that the potential of the $Fe^{2+/3+}$ redox couple is sensitive to the local environment around the iron centers.[28,29] The changes to the size of the $(Fe/M)O_4$ polyhedra resulting from the influence of "chemical pressure" from the presence of $Al^{3+}$ or $Ga^{3+}$ cations and Li substitution are therefore be expected to modify the electrochemical behavior of the system. We can keep track of these effects by calculating bond valence sums (BVS).[53] For example, the average Fe−O bond length in $NaFeO_2$ is 1.861(3) Å and the bond valence sum of the Fe cation is Fe+3.033. However, the average (Fe/Al)−O bond length in $NaFe_{0.5}Al_{0.5}O_2$ is 1.800(2) Å with a BVS = Fe+3.521, which extends to (Fe/Al)−O = 1.823(6) Å; BVS = Fe+3.366 in $LiFe_{0.5}Al_{0.5}O_2$. This net contraction in the $(Fe/Al)O_4$ coordination site will disfavor reduction of $Fe^{III}$ to $Fe^{II}$, moving the $Fe^{II/III}$ redox process to lower potential. In contrast, the average (Fe/Ga)−O bond length in $NaFe_{0.5}Ga_{0.5}O_2$ is almost unchanged (Fe/Ga−O = 1.861(3); BVS = Fe+3.05) compared to $NaFeO_2$, while that of cation ordered $LiFe_{0.5}Ga_{0.5}O_2$ is significantly larger (Fe−O = 1.897(3); BVS = Fe+2.761) favoring the reduction of $Fe^{III}$ to $Fe^{II}$, and thus raising the potential of the $Fe^{II/III}$ redox couple These effects can be seen in the electrochemical data, with the reduction of $Fe^{III}$ occurring at ∼ 3.25 V for $LiFe_{0.5}Al_{0.5}O_2$ and ∼ 3.5 V for $LiFe_{0.5}Ga_{0.5}O_2$ (Figure 8). A further consequence of the increase in the $Fe^{II/III}$ redox potential of $Li_yFe_{0.5}Ga_{0.5}O_2$ is that the system behaves as an insertion electrode in the cycling data shown in Figure 9, adopting lithium-rich compositions ($Li_yFe_{0.5}Ga_{0.5}O_2$ with $y > 1$) for the first ∼ 20 cycles − a feature that can be directly attributed to the expansion of the $FeO_4$ polyhedra which occurs on Li-for-Na cation substitution.

Chemical oxidation of $LiFe_{0.5}Al_{0.5}O_2$ and $LiFe_{0.5}Ga_{0.5}O_2$ by $NO_2BF_4$ occurs via topochemical lithium extraction. NPD data collected from $Li_{0.8}Fe_{0.5}Al_{0.5}O_2$ and $Li_{0.57}Fe_{0.5}Ga_{0.5}O_2$ reveal lithium extraction has only a small effect on the structure of the $Li_xFe_{0.5}M_{0.5}O_2$ phases, with no indication of Fe or Al/Ga cation migration, no indication of oxygen loss or transformation to a $Li(Fe/M)_5O_8$ spinel phase, as observed for unsubstituted $LiFeO_2$.[23] Reaction with LiI reintercalates some of the extracted lithium, consistent with the modest reduction potential of the $I_2/I^-$ couple (+ 3.5 V vs Li) and further indicates that the oxidized samples are lithium deficient phases, rather than the decomposition products observed on the oxidation of unsubstituted T-$LiFeO_2$.

XANES data indicate that extraction of lithium from $LiFe_{0.5}M_{0.5}O_2$ does not lead to the simple oxidation of $Fe^{III}$ to $Fe^{IV}$. A combination of O-XAS and O-RIXS suggest anion oxidation occurs to form a "hole" in a strongly hybridized Fe(3d)-O(2p) state analogous to the $3d^5\underline{L}$ states seen in phases such as $SeFeO_3$ which nominally contain $Fe^{4+}$.[50−52] This localized $Fe^{IV}$−O state appears to be inert to electrochemical reduction, leading to rapid capacity loss, as described in detail above.


https://doi.org/10.1021/acs.chemmater.4c03322
Chem. Mater. 2025, 37, 3171−3184

The "anion redox" behavior of $LiFe_{0.5}Al_{0.5}O_2$ and $LiFe_{0.5}Ga_{0.5}O_2$ show some similarities, but many contrasts to other "doped" Li−Fe−O cathode systems. For example, layered Li-rich Li−Fe−Te-O phases of approximate composition $Li_4Fe_{0.56}TeO_6$ exhibit no sign of $Fe^{III}$ to $Fe^{IV}$ oxidation on lithium extraction, in common with the $LiFe_{0.5}M_{0.5}O_2$ phases, but they do exhibit clear signatures of $O_2^-/O_2^{2-}$ molecular anion formation and release oxygen at high charging potentials.[8] In contrast, the $Li_4FeSbO_6$ system does show indications of $Fe^{III}$ to $Fe^{IV}$ oxidation on charging, but this is accompanied by of $O_2^-/O_2^{2-}$ molecular anion formation and oxygen release when charged at high potentials.[10,54] It is also observed that the reduction of the $O_2^-/O_2^{2-}$ species in $Li_{4-x}FeSbO_6$ is somewhat suppressed, so that repeated cycling accumulates these oxidized oxygen species, and depletes the lithium content of the system and thus lowers the capacity of the system in a manner somewhat analogous to that seen for $Li_xFe_{0.5}Ga_{0.5}O_2$. $Li_2FeSiO_4$ exhibits further contrasting behavior, exhibiting a large-scale structural reorganization when first one lithium is removed to form $LiFeSO_4$ and a further reorganization as further lithium is removed to form $FeSiO_4$.[11] Fe and O K-edge XANES data from $Li_{2-x}FeSiO_4$ suggest an oxidation of $Fe^{II}$ to $Fe^{III}$ associated with removal of the first lithium and then the formation of $3d^5\underline{L}$ centers on removal of the second lithium.

The diversity of electrochemical behavior of doped Li−Fe−O systems on lithium extraction suggests the electronic structures of these systems depend strongly on the identity of the dopant and the crystal structure of the doped material.

## ■ CONCLUSION

Substitution of more than 25% Al or 50% Ga for Fe in T-$LiFeO_2$ stabilizes the materials with respect to spinel conversion on lithium extraction. These cation substitutions appear to simultaneously suppress Fe-cation migration and oxygen release on cathode charging. However, the $Fe^{IV}$−O centers which form on lithium extraction are not electrochemically reduced on discharge, so accumulate in the cathode on redox cycling. Thus, we can see that while cation substitutions resolve two of the major problems associated with employing T-$LiFeO_2$ as a Li-ion cathode, the resulting $LiFe_{1-x}M_xO_2$ materials only have modest capacities which decline rapidly on cycling, highlighting the multifaceted challenges associated with Fe-based cathode materials.

## ■ ASSOCIATED CONTENT

### Supporting Information

The Supporting Information is available free of charge at https://pubs.acs.org/doi/10.1021/acs.chemmater.4c03322.

Detailed description of the structural refinements of all $NaFe_{1-x}M_xO_2$ and $LiFe_{1-x}M_xO_2$ phases ($M$ = Al, Ga) and oxidized and reduced $LiFe_{1-x}M_xO_2$ phases. ICP-MS characterization data (PDF)

## ■ AUTHOR INFORMATION


### Corresponding Author

**Michael A. Hayward** − *Department of Chemistry, University of Oxford, Inorganic Chemistry Laboratory, Oxford OX1 3QR, U.K.; The Faraday Institution, Quad One, Didcot OX11 0RA, U.K.;* orcid.org/0000-0002-6248-2063; Email: michael.hayward@chem.ox.ac.uk

### Authors

**Suraj Mahato** − *Department of Chemistry, University of Oxford, Inorganic Chemistry Laboratory, Oxford OX1 3QR, U.K.; The Faraday Institution, Quad One, Didcot OX11 0RA, U.K.;* orcid.org/0000-0002-1204-3185

**Xabier Martínez de Irujo Labalde** − *Department of Chemistry, University of Oxford, Inorganic Chemistry Laboratory, Oxford OX1 3QR, U.K.; The Faraday Institution, Quad One, Didcot OX11 0RA, U.K.*

**Heather Grievson** − *The Faraday Institution, Quad One, Didcot OX11 0RA, U.K.; Department of Materials Science and Engineering, Sir Robert Hadfield Building, University of Sheffield, Sheffield S1 3JD, U.K.*

**Josie-May Mortimer** − *The Faraday Institution, Quad One, Didcot OX11 0RA, U.K.; Department of Materials Science and Engineering, Sir Robert Hadfield Building, University of Sheffield, Sheffield S1 3JD, U.K.*

**Samuel G. Booth** − *The Faraday Institution, Quad One, Didcot OX11 0RA, U.K.; Department of Materials Science and Engineering, Sir Robert Hadfield Building, University of Sheffield, Sheffield S1 3JD, U.K.;* orcid.org/0000-0001-7643-4196

**Ashok Menon** − *The Faraday Institution, Quad One, Didcot OX11 0RA, U.K.; School of Chemistry, University College Dublin, Dublin 4, Ireland*

**Louis F. Piper** − *The Faraday Institution, Quad One, Didcot OX11 0RA, U.K.; Warwick Manufacturing Group, University of Warwick, Coventry CV4 7AL, U.K.;* orcid.org/0000-0002-3421-3210

**Serena Cussen** − *The Faraday Institution, Quad One, Didcot OX11 0RA, U.K.; School of Chemistry, University College Dublin, Dublin 4, Ireland*

Complete contact information is available at: https://pubs.acs.org/10.1021/acs.chemmater.4c03322


### Author Contributions

The manuscript was written through contributions of all authors

### Notes

The authors declare no competing financial interest.

## ■ ACKNOWLEDGMENTS

This work was supported by the Faraday Institution project FutureCat (Grant No. FIRG017). Diffraction experiments at the Diamond Light Source were performed as part of the Block Allocation Group award "Oxford Solid State Chemistry BAG to probe composition-structure-property relationships in solids" (CY25166). We thank the Diamond Light Source for the award of XAS beam time as part of the Energy Materials Block Allocation Group SP14239. Experiments at the ISIS pulsed neutron facility were supported by a beam time allocation from the STFC (DOI 10.5286/ISIS.E.RB2220059). SM thanks the Clarendon Fund, University of Oxford for a scholarship.

## ■ REFERENCES


(1) Whittingham, M. S. Lithium batteries and cathode materials. *Chem. Rev.* **2004**, *104* (10), 4271−4301.

(2) Whittingham, M. S. Ultimate Limits to Intercalation Reactions for Lithium Batteries. *Chem. Rev.* **2014**, *114* (23), 11414−11443.

(3) Liu, J.; Bao, Z. N.; Cui, Y.; Dufek, E. J.; Goodenough, J. B.; Khalifah, P.; Li, Q. Y.; Liaw, B. Y.; Liu, P.; Manthiram, A.; Meng, Y. S.; Subramanian, V. R.; Toney, M. F.; Viswanathan, V. V.;

Whittingham, M. S.; Xiao, J.; Xu, W.; Yang, J. H.; Yang, X. Q.; Zhang, J. G. Pathways for practical high-energy long-cycling lithium metal batteries. *Nat. Energy* **2019**, *4* (3), 180−186.

(4) Li, M.; Lu, J. Cobalt in lithium-ion batteries. *Science* **2020**, *367* (6481), 979−980.

(5) Booth, S. G.; Nedoma, A. J.; Anthonisamy, N. N.; Baker, P. J.; Boston, R.; Bronstein, H.; Clarke, S. J.; Cussen, E. J.; Daramalla, V.; De Volder, M.; et al. Perspectives for next generation lithium-ion battery cathode materials. *APL Mater.* **2021**, *9* (10), 109201.

(6) Takeda, Y.; Naka, S.; Takano, M.; Shinjo, T.; Takada, T.; Shimada, M. Preparation and characterization of stoichiometric $CaFeO_3$. *Mater. Res. Bull.* **1978**, *13* (1), 61−66.

(7) Bocquet, A. E.; Fujimori, A.; Mizokawa, T.; Saitoh, T.; Namatame, H.; Suga, S.; Kimizuka, N.; Takeda, Y.; Takano, M. Electronic structure of $SrFe^{4+}O_3$ and related Fe perovskite oxides. *Phys. Rev. B* **1992**, *45* (4), 1561−1570.

(8) McCalla, E.; Prakash, A. S.; Berg, E.; Saubanère, M.; Abakumov, A. M.; Foix, D.; Klobes, B.; Sougrati, M. T.; Rousse, G.; Lepoivre, F.; Mariyappan, S.; Doublet, M. L.; Gonbeau, D.; Novak, P.; Van Tendeloo, G.; Hermann, R. P.; Tarascon, J. M. Reversible Li-Intercalation through Oxygen Reactivity in Li-Rich Li-Fe-Te Oxide Materials. *J. Electrochem. Soc.* **2015**, *162* (7), A1341−A1351.

(9) McCalla, E.; Abakumov, A. M.; Saubanère, M.; Foix, D.; Berg, E. J.; Rousse, G.; Doublet, M. L.; Gonbeau, D.; Novák, P.; Van Tendeloo, G.; Dominko, R.; Tarascon, J. M. Visualization of O-O peroxo-like dimers in high-capacity layered oxides for Li-ion batteries. *Science* **2015**, *350* (6267), 1516−1521.

(10) McCalla, E.; Sougrati, M. T.; Rousse, G.; Berg, E. J.; Abakumov, A.; Recham, N.; Ramesha, K.; Sathiya, M.; Dominko, R.; Van Tendeloo, G.; Novak, P.; Tarascon, J. M. Understanding the Roles of Anionic Redox and Oxygen Release during Electrochemical Cycling of Lithium-Rich Layered $Li_4FeSbO_6$. *J. Am. Chem. Soc.* **2015**, *137* (14), 4804−4814.

(11) Masese, T.; Tassel, C.; Orikasa, Y.; Koyama, Y.; Arai, H.; Hayashi, N.; Kim, J.; Mori, T.; Yamamoto, K.; Kobayashi, Y.; Kageyama, H.; Ogumi, Z.; Uchimoto, Y. Crystal Structural Changes and Charge Compensation Mechanism during Two Lithium Extraction/Insertion between $Li_2FeSiO_4$ and $FeSiO_4$. *J. Phys. Chem. C* **2015**, *119* (19), 10206−10211.

(12) Shannon, R. D. Revised effective ionic radii. *Acta Crystallogr.* **1976**, *A32*, 751−766.

(13) Li, J. G.; Li, J. J.; Luo, J.; Wang, L.; He, X. M. Recent Advances in the LiFeO2-based Materials for Li-ion Batteries. *Int. J. Electrochem. Sci.* **2011**, *6* (5), 1550−1561.

(14) Kanno, R.; Shirane, T.; Kawamoto, Y.; Takeda, Y.; Takano, M.; Ohashi, M.; Yamaguchi, Y. Synthesis, structure, and electrochemical properties of a new lithium iron oxide, $LiFeO_2$, with a corrugated layer structure. *J. Electrochem. Soc.* **1996**, *143* (8), 2435−2442.

(15) Wang, M. J.; Navrotsky, A. $LiMO_2$ (M = Mn, Fe, and Co): Energetics, polymorphism and phase transformation. *J. Solid State Chem.* **2005**, *178* (4), 1230−1240.

(16) Abdel-Ghany, A. E.; Mauger, A.; Groult, H.; Zaghib, K.; Julien, C. M. Structural properties and electrochemistry of alpha-$LiFeO_2$. *J. Power Sources* **2012**, *197*, 285−291.

(17) Barre, M.; Catti, M. Neutron diffraction study of the beta' and gamma phases of $LiFeO_2$. *J. Solid State Chem.* **2009**, *182* (9), 2549−2554.

(18) Guo, S. P.; Ma, Z.; Li, J. C.; Xue, H. G. First investigation of the electrochemical performance of gamma-$LiFeO_2$ micro-cubes as promising anode material for lithium-ion batteries. *J. Mater. Sci.* **2017**, *52* (3), 1469−1476.

(19) Sakurai, Y.; Arai, H.; Yamaki, J. Preparation of electrochemically active alpha-$LiFeO_2$ at low temperature. *Solid State Ionics* **1998**, *113−115*, 29−34.

(20) Morales, J.; Santos-Pena, J. Highly electroactive nanosized alpha-$LiFeO_2$. *Electrochem. Commun.* **2007**, *9* (8), 2116−2120.

(21) Kanno, R.; Shirane, T.; Inaba, Y.; Kawamoto, Y. Synthesis and electrochemical properties of lithium iron oxides with layer-related structures. *J. Power Sources* **1997**, *68* (1), 145−152.

(22) Shirane, T.; Kanno, R.; Kawamoto, Y.; Takeda, Y.; Takano, M.; Kamiyama, T.; Izumi, F. Structure and Physical-Properties of Lithium Iron-Oxide, $LiFeO_2$, Synthesized by Ionic Exchange-Reaction. *Solid State Ionics* **1995**, *79*, 227−233.

(23) Armstrong, A. R.; Tee, D. W.; La Mantia, F.; Novak, P.; Bruce, P. G. Synthesis of tetrahedral $LiFeO_2$ and its behavior as a cathode in rechargeable lithium batteries. *J. Am. Chem. Soc.* **2008**, *130* (11), 3554−3559.

(24) Lee, Y. S.; Sato, S.; Sun, Y. K.; Kobayakawa, K.; Sato, Y. A new type of orthorhombic $LiFeO_2$ with advanced battery performance and its structural change during cycling. *J. Power Sources* **2003**, *119*, 285−289.

(25) Lee, Y. S.; Sato, S.; Tabuchi, M.; Yoon, C. S.; Sun, Y. K.; Kobayakawa, K.; Sato, Y. Structural change and capacity loss mechanism in orthorhombic Li/$LiFeO_2$ system during cycling. *Electrochem. Commun.* **2003**, *5* (7), 549−554.

(26) Hirayama, M.; Tomita, H.; Kubota, K.; Kanno, R. Structure and electrode reactions of layered rocksalt $LiFeO_2$ nanoparticles for lithium battery cathode. *J. Power Sources* **2011**, *196* (16), 6809−6814.

(27) Catti, M.; Montero-Campillo, M. First-principles modelling of lithium iron oxides as battery cathode materials. *J. Power Sources* **2011**, *196* (8), 3955−3961.

(28) Martinez de Irujo-Labalde, X.; Grievson, H.; Mortimer, J. M.; Booth, S. G.; Scrimshire, A.; Bingham, P. A.; Suard, E.; Cussen, S. A.; Hayward, M. A. Suppression of Fe-Cation Migration by Indium Substitution in $LiFe_{2-x}In_xSbO_6$ Cathode Materials. *Chem. Mater.* **2023**, *35* (1), 337−346.

(29) Martinez de Irujo-Labalde, X.; Lee, M. Y.; Grievson, H.; Mortimer, J. M.; Booth, S. G.; Suard, E.; Cussen, S. A.; Hayward, M. A. Influence of Cation Substitution on Cycling Stability and Fe-Cation Migration in $Li_3Fe_{3-x}M_xTe_2O_{12}$ (M = Al, In) Cathode Materials. *Inorg. Chem.* **2024**, *63* (2), 1395−1403.

(30) Coelho, A. A. TOPAS and TOPAS-Academic: An optimization program integrating computer algebra and crystallographic objects written in C plus. *J. Appl. Crystallogr.* **2018**, *51*, 210−218.

(31) Ravel, B.; Newville, M. ATHENA and ARTEMIS: Interactive graphical data analysis using IFEFFIT. *Phys. Scr.* **2005**, *T115*, 1007−1010.

(32) Zhou, K.-J.; Walters, A.; Garcia-Fernandez, M.; Rice, T.; Hand, M.; Nag, A.; Li, J.; Agrestini, S.; Garland, P.; Wang, H.; Alcock, S.; Nistea, I.; Nutter, B.; Rubies, N.; Knap, G.; Gaughran, M.; Yuan, F.; Chang, P.; Emmins, J.; Howell, G. I21: An advanced high-resolution resonant inelastic X-ray scattering beamline at Diamond Light Source. *J. Synchrotron Radiat.* **2022**, *29* (2), 563−580.

(33) Basham, M.; Filik, J.; Wharmby, M. T.; Chang, P. C. Y.; El Kassaby, B.; Gerring, M.; Aishima, J.; Levik, K.; Pulford, B. C. A.; Sikharulidze, I.; Sneddon, D.; et al. Ashtona Data Analysis WorkbeNch (DAWN). *J. Synchrotron Radiat.* **2015**, *22*, 853−858.

(34) Grey, I. E.; Hill, R. J.; Hewat, A. W. A neutron powder diffraction study of the $\beta$ to $\gamma$ phase transformation in $NaFeO_2$. *Z. Kristallogr. -Cryst. Mater.* **1990**, *193* (1−4), 51−69.

(35) Bara, J. J.; Bogacz, B. F.; Jaworska, T.; Leciejewicz, J.; Styczynska, M.; Szytula, A. Crystal and magnetic properties of $NaFe_{1-x}Al_xO_2$ solid solutions. *J. Magn. Magn. Mater.* **1988**, *75* (1−2), 73−78.

(36) Plattner, E.; Vollenke, H.; Wittmann, A. Crystal structure of compound $Li_2ZnGeO_4$. *Monatsh. Chem.* **1976**, *107* (4), 921−927.

(37) Sears, V. F. Neutron Scattering Lengths and Cross Sections. *Neutron News* **1992**, *3*, 26−37.

(38) Degroot, F. M. F.; Grioni, M.; Fuggle, J. C.; Ghijsen, J.; Sawatzky, G. A.; Petersen, H. Oxygen 1s X-ray absorption edges of Transition-metal oxides. *Phys. Rev. B* **1989**, *40* (8), 5715−5723.

(39) Wu, J. P.; Li, Q. H.; Sallis, S.; Zhuo, Z. Q. Q.; Gent, W. E.; Chueh, W. C.; Yan, S. S.; Chuang, Y. D.; Yang, W. L. Fingerprint Oxygen Redox Reactions in Batteries through High-Efficiency Mapping of Resonant Inelastic X-ray Scattering. *Condens. Matter* **2019**, *4* (1), 5.

(40) Wu, J.; Yang, Y.; Yang, W. L. Advances in soft X-ray RIXS for studying redox reaction states in batteries. *Dalton Trans.* **2020**, *49* (39), 13519−13527.
(41) Hu, Y.; Liu, T. F.; Cheng, C.; Yan, Y. Y.; Ding, M. L.; Chan, T. S.; Guo, J. H.; Zhang, L. Quantification of Anionic Redox Chemistry in a Prototype Na-Rich Layered Oxide. *ACS Appl. Mater. Interfaces* **2020**, *12* (3), 3617−3623.
(42) Xu, J.; Sun, M. L.; Qiao, R. M.; Renfrew, S. E.; Ma, L.; Wu, T. P.; Hwang, S.; Nordlund, D.; Su, D.; Amine, K.; et al. Elucidating anionic oxygen activity in lithium-rich layered oxides. *Nat. Commun.* **2018**, *9*, 947.
(43) Sathiya, M.; Rousse, G.; Ramesha, K.; Laisa, C. P.; Vezin, H.; Sougrati, M. T.; Doublet, M. L.; Foix, D.; Gonbeau, D.; Walker, W.; Prakash, A. S.; Ben Hassine, M.; Dupont, L.; Tarascon, J. M. Reversible anionic redox chemistry in high-capacity layered-oxide electrodes. *Nat. Mater.* **2013**, *12* (9), 827−835.
(44) Taylor, Z. N.; Perez, A. J.; Coca-Clemente, J. A.; Braga, F.; Drewett, N. E.; Pitcher, M. J.; Thomas, W. J.; Dyer, M. S.; Collins, C.; Zanella, M.; Johnson, T.; Day, S.; Tang, C.; Dhanak, V. R.; Claridge, J. B.; Hardwick, L. J.; Rosseinsky, M. J. Stabilization of O-O Bonds by $d^0$ Cations in $Li_{4+x}Ni_{1-x}WO_6$ ($0 \leq x \leq 0.25$) Rock Salt Oxides as the Origin of Large Voltage Hysteresis. *J. Am. Chem. Soc.* **2019**, *141* (18), 7333−7346.
(45) Oishi, M.; Yamanaka, K.; Watanabe, I.; Shimoda, K.; Matsunaga, T.; Arai, H.; Ukyo, Y.; Uchimoto, Y.; Ogumi, Z.; Ohta, T. Direct observation of reversible oxygen anion redox reaction in Li-rich manganese oxide, $Li_2MnO_3$, studied by soft X-ray absorption spectroscopy. *J. Mater. Chem. A* **2016**, *4* (23), 9293−9302.
(46) Luo, K.; Roberts, M. R.; Hao, R.; Guerrini, N.; Pickup, D. M.; Liu, Y. S.; Edström, K.; Guo, J. H.; Chadwick, A. V.; Duda, L. C.; Bruce, P. G. Charge-compensation in 3d-transition-metal-oxide intercalation cathodes through the generation of localized electron holes on oxygen. *Nat. Chem.* **2016**, *8* (7), 684−691.
(47) Luo, K.; Roberts, M. R.; Guerrini, N.; Tapia-Ruiz, N.; Hao, R.; Massel, F.; Pickup, D. M.; Ramos, S.; Liu, Y. S.; Guo, J. H.; Chadwick, A. V.; Duda, L. C.; Bruce, P. G. Anion Redox Chemistry in the Cobalt Free 3d Transition Metal Oxide Intercalation Electrode Li $Li_{0.2}Ni_{0.2}Mn_{0.6}O_2$. *J. Am. Chem. Soc.* **2016**, *138* (35), 11211−11218.
(48) Hu, E. Y.; Li, Q. H.; Wang, X. L.; Meng, F. Q.; Liu, J.; Zhang, J. N.; Page, K.; Xu, W. Q.; Gu, L.; Xiao, R. J.; Li, H.; Huang, X. J.; Chen, L. Q.; Yang, W. L.; Yu, X. Q.; Yang, X. Q. Oxygen-redox reactions in $LiCoO_2$ cathode without O-O bonding during charge-discharge. *Joule* **2021**, *5* (3), 720−736.
(49) House, R. A.; Rees, G. J.; McColl, K.; Marie, J. J.; Garcia-Fernandez, M.; Nag, A.; Zhou, K. J.; Cassidy, S.; Morgan, B. J.; Islam, M. S.; et al. Delocalized electron holes on oxygen in a battery cathode. *Nat. Energy* **2023**, *8* (4), 351−360.
(50) Abbate, M.; Zampieri, G.; Okamoto, J.; Fujimori, A.; Kawasaki, S.; Takano, M. X-ray absorption of the negative charge-transfer material $SrFe_{1-x}Co_xO_3$. *Phys. Rev. B* **2002**, *65* (16), 165120.
(51) Chen, W. -T.; Saito, T.; Hayashi, N.; Takano, M.; Shimakawa, Y. Ligand-hole localization in oxides with unusual valence Fe. *Sci. Rep.* **2012**, *2*, 449.
(52) Kitou, S.; Gen, M.; Nakamura, Y.; Sugimoto, K.; Tokunaga, Y.; Ishiwata, S.; Arima, A. T.-H. Real-Space Observation of Ligand Hole State in Cubic Perovskite $SrFeO_3$. *Adv. Sci.* **2023**, *10* (29), 2302839.
(53) Brese, N. E.; O'Keeffee, M. Bond-Valence Parameters for Solids. *Acta Crystallogr., Sect. B: Strucut. Sci.* **1991**, *B47*, 192−197.
(54) McCalla, E.; Abakumov, A.; Rousse, G.; Reynaud, M.; Sougrati, M. T.; Budic, B.; Mahmoud, A.; Dominko, R.; Van Tendeloo, G.; Hermann, R. P.; Tarascon, J. M. Novel Complex Stacking of Fully-Ordered Transition Metal Layers in $Li_4FeSbO_6$ Materials. *Chem. Mater.* **2015**, *27* (5), 1699−1708.


https://doi.org/10.1021/acs.chemmater.4c03322
*Chem. Mater.* 2025, 37, 3171−3184